YoungSol Kim

Assessment of the impact of acquisition configuration of CO2 detection inspired by Top Layer at Sleipner

Petroleum Geophysics

Master's thesis in Petroleum Geophysics
Supervisor: Philip Ringrose
Co-supervisor: Ricardo Jose Martinez Guzman
Industry advisor: Thomas Elboth, Shearwater June 2023

Norwegian University of Science and Technology
Faculty of Engineering
Department of Geosciences and Petroleum

NTNU

ABSTRACT

This thesis examines the role of seismic acquisition geometry in the detection of carbon dioxide (CO2) layers in various scenarios. Carbon capture and storage (CCS) technologies are being investigated due to the pressing need to address climate change, and accurate monitoring of CO2 leaks is essential for the safety and effectiveness of storage sites. The study compares three scenarios: the absence of a CO2 layer, the presence of a CO2 layer of true depth, a CO2 layer of shallower depth.

The research begins with the generation of velocity models using the wave equation and specific parameters to represent various scenarios of CO2 accumulation and leakage; P-wave reflections are primarily used. Despite the fact that the models used in this study are based on simplified environments and single-source configurations, they provide valuable insights into the behavior of CO2 in the subsurface. The emphasis on cost-effectiveness includes grid size, time step, and spatial sampling for model design.

It is important to acknowledge the study's limitations. The lack of specific rock properties and comprehensive seismic processing techniques has a negative effect on the precision and quality of the results. Despite these limitations, the study demonstrates the fundamental concept of CO2 layer detection and sequential CO2 injection phases.

The difference in two-way travel time (TWT) between the top and bottom of the CO2 layer is an interesting observation. The 800 m CO2 layer model displayed a TWT difference of 60 ms at zero offset, which decreased to 51 ms at the last receiver offset. The shallower depth 400 m CO2 layer model displayed a TWT difference of 60 ms at zero offsets, which decreased to 45 ms at the final receiver offset. The decrease in TWT with increasing offset suggests that a CO2 layer of shallower depth has a shorter ray path, highlighting the importance of subsurface properties, such as the overburden layer, in the detection process.

CONTENTS

LIST OF FIGURES

LIST OF TABLES

ABBREVIATIONS

List of all abbreviations in alphabetic order:

- **CCS** Carbon Capture and Storage
- **CO2** Carbon dioxide
- **RTM** Reverse Time Migration
- **NTNU** Norwegian University of Science and Technology
- **FFT** Fast Fourier Transform
- **TWT** Two Way Travel time

CHAPTER

ONE

INTRODUCTION

As a strategy to reduce greenhouse gas emissions, carbon capture and storage (CCS) technologies is being investigated and developed. CCS involves the capture, transport, and secure underground storage of carbon dioxide (CO2) to prevent its release into the atmosphere.

Precise detection and monitoring of potential CO2 leaks are crucial to the effective implementation of CCS technologies. CO2 detection benefit from insights and methodologies derived from prior research and industry practices. For the detecting methods are based on seismic data acquisition and imaging interpretation [6]. Existing solutions to monitor CO2 sequestration projects typically rely on seismic methods, such as time-lapse seismic surveying [13]. The application of these techniques to CCS projects requires careful consideration of the unique characteristics of CO2 storage reservoirs [15].

Despite advancements in CO2 detection methods, a number of limitations remain. Variations in CO2 migration patterns, reservoir heterogeneity, and the need for long-term monitoring are challenges unique to CO2 storage reservoirs. Additionally, when it comes to CCS projects, it is hard to apply directly. In order to ensure the scalability and economic viability of CCS technologies, the cost must be reduced.

The difficulty lies in developing acquisition configurations that detect CO2 leaks in a variety of scenarios while taking into account the limitations of existing hardware. The objective is to improve the precision, dependability, and cost-effectiveness of monitoring systems in order to ensure the safe and efficient operation of CCS projects [1].

The primary objective of this thesis is to evaluate the effect of acquisition configuration on CO2 detection by comparing three distinct scenarios: true depth CO2 layer, shallower depth CO2 layer, and no CO2 layer.

The specific objectives are:

- Deigning a cost-effective acquisition and imaging system that is able to detect thin layer of CO2 developed in subsurface aquifers.
- Extracting quantitative properties from the reservoir and the CO2 layers.
- Identifying the key factors influencing the detection of CO2 leaks and understanding their impact on monitoring performance.

To accomplish these objectives, I will combine theoretical analysis, numerical modeling, and data analysis. The theoretical analysis will consist of a review of existing literature, an examination of the principles of CO2 detection, and an understanding of the limitations of existing monitoring techniques. Numerical modeling is used to simulate how CO2 acts in different situations so that different acquisition configurations can be tested.

This research aims to provide valuable insights into the impact of acquisition configuration on CO2 detection and provide recommendations for optimizing monitoring systems in CCS projects. The findings of this thesis will ultimately contribute to ongoing efforts to improve the safety, efficiency, and scalability of CCS technologies, thereby facilitating the global transition to a sustainable and low-carbon future.

1.1 Motivation

This thesis is motivated by the urgent need to develop effective carbon capture and storage (CCS) technologies as a climate change mitigation strategy. By capturing and storing carbon dioxide (CO2) from industrial processes and power generation, CCS offers the potential to significantly reduce greenhouse gas emissions [15]. However, accurate and reliable CO2 detection and monitoring systems are essential to the successful implementation of CCS.

In addition, desire to address the existing knowledge gaps and difficulties associated with CO2 detection in CCS projects was my personal motivation. Although considerable research has been conducted in this field, it is still necessary to evaluate the effect of various acquisition configurations on our ability to detect CO2. By focusing on three distinct scenarios — true depth CO2 layer, shallower depth CO2 layer, and no CO2 layer — this study aims to provide insights that can be used to inform the design and optimization of monitoring systems.

By recognizing the advantages and disadvantages of various acquisition configurations, we can identify areas for enhancement and improve the overall accuracy and dependability of CO2 detection systems to reduce cost. Conditions of storage may not always correspond to the ideal scenario. The presence of a CO2 layer at a shallower depth or the absence of a CO2 layer complicates and complicates the detection of subsurface formation.

The objective of this thesis is to advance the understanding of CO2 detection in CCS projects by conducting an analysis of the impact of acquisition configuration. This research's findings and insights have the potential to drive improvement in monitoring systems, thereby contributing to the widespread adoption of CCS technologies. By improving the precision, dependability, and cost-effectiveness of CO2 detection, we can aid global efforts to combat climate change and transition to a more sustainable future.

1.2 Project description

This project aims to propose designs for accurate and cost-effective monitoring of carbon dioxide (CO2) sequestration projects.

In the absence of a CO2 layer scenario, seismic surveying methods will be evaluated to reduce false positives and misinterpretations. This scenario is the background scenario which indicates before CO2 injection. Also, the scenario intends to ensure that the monitoring systems can distinguish between the presence and absence of a CO2 layer in the subsurface aquifer.

In the true depth CO2 layer scenario, the objective of the scenario is to accurately evaluate the conformance of CO2 within the subsurface aquifer. This scenario is after CO2 injection phase and aims to optimize the precision and resolution of seismic data in order to precisely locate CO2 within the aquifer and track its migration over time [13]. This scenario is consistent with the goal of ensuring that CO2 behaves as predicted by forecasting engines, thereby establishing a baseline for efficient monitoring.

Due to the close proximity of CO2 to potential leakage pathways, the scenario of a CO2 layer with a shallow depth poses some challenges. The project will investigate seismic surveying techniques to confirm that CO2 is contained within the aquifer and prevent its migration beyond the aquifer's boundaries [12]. We try to determine to improve the ability to monitor and detect potential CO2 leaks in scenarios where the CO2 layer is located at a shallower depth by analyzing different seismic acquisition configurations.

Using a multidisciplinary approach that incorporates geology, geophysics, engineering, and data analysis, the project will investigate seismic acquisition technologies and data processing techniques. The collected seismic data will be subjected statistical analysis, data visualization, and studies to determine the efficacy of various seismic survey configurations for each scenario.

The project will also consider the cost-effectiveness and practicability of conducting high-quality seismic surveys. By striking a balance between data quality and costs, the project aims to develop scalable and economically viable CO2 sequestration monitoring techniques.

This project's outcomes will hopefully aid CO2 sequestration monitoring practices by enhancing the precision and dependability of seismic surveys in the three identified scenarios. Ultimately, this project will support the successful implementation of CO2 sequestration as a crucial strategy for combating climate change.

CHAPTER

TWO

THEORY

2.1 Seismic Modelling

Beginning with a given geological model of the subsurface, seismic modeling is a process. Simulation may be a more appropriate term than modeling for this field, since we are simulating using wave equations the propagation of seismic waves through the earth. To perform seismic modeling, we must simplify both the subsurface and the procedure for wave propagation. Giving enough time on can create a very complicated an detailed model of the subsurface. But in terms of cost-effectiveness, it is more reasonable to divide the earth into distinct layers or volumes to which we can assign roughly equivalent properties. We have the acoustic case if we only specify density and P-wave velocity for each volume (or layer) in our model. In this case, we also assume that the earth is isotropic, meaning that there are no changes in parameter values based on the direction of wave propagation. If the S-wave velocity for each volume of our geological model is also specified, we are speaking of elastic modeling. Acoustic and elastic modelling are two major types of seismic modelling. A model that incorporates anisotropy is referred to as, for example, elastic anisotropic modelling, or if absorption effects are considered, visco-elastic modelling may be used.

Since a scaled-down version of a real seismic experiment is being simulated, physical experiments conducted on small-scale synthetic models are frequently referred to as seismic modelling. Experiments of this nature are useful for testing different processing algorithms on a known earth model and calibrating and verifying numerical schemes used to simulate seismic wave propagation through the earth.

There are numerous reasons to perform seismic modeling:

1) For well connection and calibration purposes. To properly interpret seismic data between well locations, it is essential to comprehend the relationship between seismic data and changes in lithology and saturation within a well.
2) Methods of wave extrapolation are essential for seismic migration.
3) The vast majority of feasibility studies are associated with a time lapse seismic study involve seismic modeling of pre- and post-production scenarious, which is frequently based on fluid flow simulations.

2.1.1 Seismic wave propagation

Seismic wave propagation is the process by which waves generated by an energy source, such as an earthquake or an artificial seismic source, travel through the subsurface of the Earth. These waves carry valuable information about the properties and structures of the subsurface, allowing us to study and comprehend the interior of the Earth. (Figure 2.1.1).

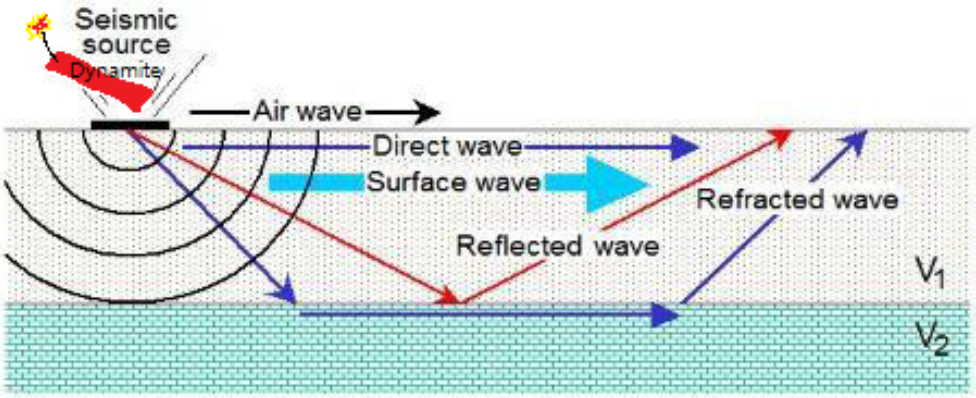

Figure 2.1.1: Basic concept of seismic survey.

There are two primary types of seismic waves: surface waves and body waves. Additional classifications of body waves include primary waves (P-waves) and secondary waves (S-waves). P-waves are compressional waves that travel through solid, liquid, and gaseous substances. Following an earthquake, they have the fastest velocity and are the first to arrive at a seismic station. S-waves are shear waves that only travel through solid materials. They travel more slowly than P-waves, arriving at seismic stations after P-waves.

As their name suggests, surface waves propagate along the Earth's surface or along an interface. They are typically slower than both P-waves and S-waves, but they can cause greater ground movement and damage during an earthquake. Love waves and Rayleigh waves are two additional classifications of surface waves. Love waves have a horizontal motion perpendicular to the direction of propagation, whereas Rayleigh waves roll like ocean waves.

Seismic waves penetrate the subsurface and interact with various geological formations and structures. These interactions modify the waves' direction, velocity, and amplitude. Geoscientists can interpret the subsurface characteristics, such as the composition, density, and layering of rocks, as well as the presence of geological features such as faults, fractures, and subsurface fluid reservoirs, by analyzing the properties of seismic waves recorded by seismometers at different locations.

Seismic wave propagation is fundamental to numerous geophysical applications, including earthquake research, exploration for natural resources (such as oil, gas, and minerals), and imaging of the subsurface for engineering purposes. Seismic surveys are carried out by deploying seismic sources such as explosives or vibrating trucks. Also, airguns are commonly used as seismic sources in offshore seismic surveys because of their efficiency. And arrays of seismometers record waves propagating through the Earth. Using sophisticated techniques, the

recorded data are then processed and analyzed to generate detailed subsurface images and models.

The velocity of a P-wave is related to the bulk modulus (K) and the shear modulus (μ) in the following way [6].

$$V_p = \sqrt{\frac{K + \frac{4}{3}\mu}{\rho}} = \sqrt{\frac{\lambda + 2\mu}{\rho}} \tag{2.1}$$

where ρ is the density and λ is Lames first constant. For an isotropic medium, the velocity of shear waves is simply given by

$$V_s = \sqrt{\frac{\mu}{\rho}} \tag{2.2}$$

Since the shear modulus of water is zero, propagation of shear waves in water is impossible. Since they cannot be directly measured, shear waves do not play a significant role in conventional marine streamer surveys. But they are recorded on nodes.

2.1.1.1 Snell's law

When a wave crosses a boundary between two isotropic media, its direction changes such that the ratio between the sine of the ray-angle and the medium velocity is maintained. This is Snell's law, and it applies to S- and P-waves, as well as both transmitted and reflected waves. In addition, when attempting to calculate the critical angle and critical offset based on the geometry of the setup, Snell's law is predominantly applied. Describe Snell's law for the ray shown in Figure 2.1.2.

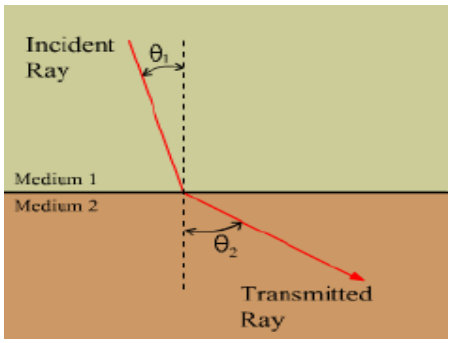

Figure 2.1.2: Basic concept of Snell's law.

$$\frac{sin\theta_1}{V_1} = \frac{sin\theta_2}{V_2} = p \tag{2.3}$$

This ratio is also called the ray parameter p.

When an elastic body wave encounters an interface and the deeper medium has the highest velocity, a refracted wave or head wave can be produced. Such a wave propagates in the high-velocity medium and parallel to the bedding like an interface wave. As it propagates along the interface, it emits energy as free body waves. (Figure 2.1.3).

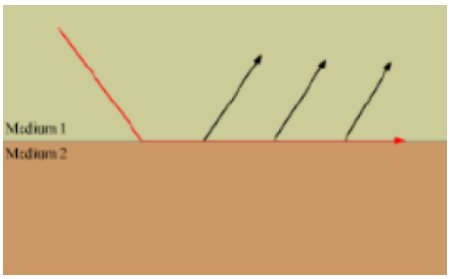

Figure 2.1.3: Refracted wave generated when the wave hits deeper and higher medium.

The angle of incidence must be equal to the critical angle (i_c) before a head wave can be generated. This angle is calculable using Snell's law in Figure 2.1.4.

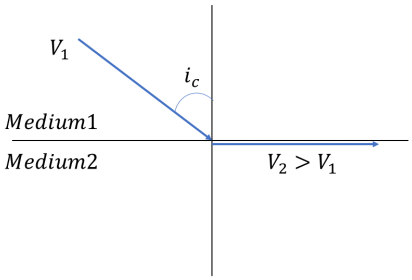

Figure 2.1.4: When the angle of incidence is equal to the critical angle.

$$\frac{sin(i_c)}{V_1} = \frac{sin90\circ}{V_2} \Rightarrow sin(i_c) = \frac{V_1}{V_2} \tag{2.4}$$

2.1.2 Seismic data acquisition

It is possible to create a detailed image of the subsurface, including the location and shape of geological features, by analyzing the travel times and amplitudes of the reflected seismic waves. Receivers that are located along lines (2D seismics) or on a grid (3D seismics) measure the reflected wavefield. This data can be utilized to identify and evaluate the stability of subsurface structures. CO2 sequestration projects can use marine seismic data acquisition to detect carbon dioxide (CO2) layers beneath the seafloor (Figure 2.1.5). When it comes to monitoring and confirming the containment of CO2 within subsurface aquifers, marine seismic surveys provide valuable information regarding the distribution, extent, and behavior of the CO2 plume.

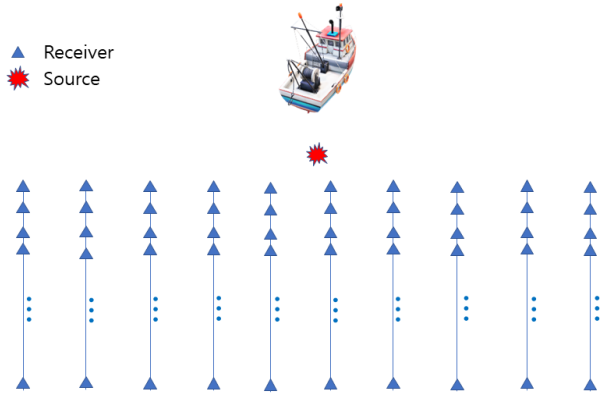

Figure 2.1.5: Schematic view of marine seismic data acquisition.

In the context of CO2 sequestration monitoring, the process of acquiring marine seismic data for CO2 detection includes the following factors [7]:

Survey Design: The survey design is tailored to CO2 detection's specific objectives. It consists of identifying the survey area, planning the source and receiver configurations, and selecting the acquisition parameters. The objective is to collect data that captures the CO2 layer with sufficient resolution and coverage.

Seismic Source: The choice of seismic source is contingent on variables such as the CO2 layer's thickness, the desired penetration depth, and environmental considerations. In marine CO2 detection surveys, air guns are common source. The source emits seismic waves that penetrate the seafloor and propagate through the water column, interacting with the CO2 layer.

Receiver Array: A receiver array composed of hydrophones or geophones is deployed in the water column to capture seismic waves reflected and refracted by subsurface layers, including the CO2 layer.

Data Acquisition: The seismic source is activated, and the receiver array records the seismic waves generated by the source as well as their interaction with the subsurface, including the CO2 layer. To accurately correlate recorded data with specific locations on the seafloor, precise navigation and positioning are needed.

2.1.3 Seismic data processing

Seismic data processing refers to a series of steps and techniques applied to raw seismic data in order to improve its quality, eliminate noise, and extract subsurface-relevant information. The objective of seismic data processing is to produce a clearer and more precise image of subsurface structures and geological features [8].

Typically, the seismic data processing workflow consists of the following steps:

1. Data Quality Control: The first step entails evaluating the acquired seismic data's quality. This includes examining for issues such as instrument failures,

timing errors, insufficient coverage, and significant noise contamination. Any problematic data segments may be flagged for additional analysis or possible deletion [6][7].

2. Data Preprocessing:

- Noise Removal: Various noise removal techniques are applied to eliminate unwanted noise sources, such as ambient noise, ground roll, or instrument noise. To suppress noise components while preserving the desired seismic signals, filtering techniques such as frequency-based filters (e.g., high-pass, low-pass, band-pass), spectral subtraction, and statistical methods are utilized.

3. Data Enhancement:

- Deconvolution: Deconvolution techniques aim to improve the resolution of seismic data by removing the effects of the seismic wavelet, which represents the source signature or the earth's response. Methods for deconvolution consist of inverse filtering, wavelet shaping, and statistical deconvolution.

- Filtering: Filtering modifies the frequency content of seismic data. It assists in enhancing desired signals or suppressing undesirable frequencies, such as noise or high-frequency noise components. Low-pass, high-pass, band-pass, and notch filters are typical filter configurations.

- Velocity analysis: Velocity analysis is a step in seismic data processing that aims to determine the correct seismic wave velocity variation within the subsurface. This is for imaging and interpretation of the subsurface structures.

- Demultiple: Demultiple is a technique used to remove unwanted multiple reflections from seismic data. Multiple reflections occur when seismic waves bounce off subsurface layers multiple times before reaching the seismometers. These multiples can interfere with the primary reflections, making it challenging to interpret the seismic data accurately.

4. Data Migration: Migration is a step in the processing of seismic data that aims to create an accurate image of subsurface structures. It involves extrapolating seismic wavefields and adjusting for wave propagation effects. Migration techniques, such as Kirchhoff migration and Reverse Time Migration (RTM), help accurately position reflectors and provide a more precise representation of subsurface features.

Processing seismic data is a complex and iterative procedure that requires knowledge of signal processing, mathematics, and geophysics. It entails applying various algorithms, filters, and imaging techniques to transform raw seismic data into a more accurate representation of the subsurface. The processed data provides valuable insights into the geological properties, thereby facilitating decision-making processes for oil and gas exploration, reservoir characterization, and geohazard assessment.

2.1.3.1 Fourier transform

In seismic processing, the Fourier transform is a fundamental mathematical tool used to analyze and manipulate seismic data in the frequency domain. It enables

the transformation of seismic data from the time domain to the frequency domain, allowing for a variety of data analysis, filtering, and imaging techniques. Let us transform a function g(t), where t represents time, into the transform-variable domain, the frequency-domain [7].

$$G(f) = \int_{-\infty}^{+\infty} g(t) exp(-2\pi i f t) dt \tag{2.5}$$

where i is the imaginary unit, and f is the transform variable frequency.

The expression for the inverse transform, the reconstruction of the time signal from its frequency components, is as follows:

$$g(t) = \int_{-\infty}^{+\infty} G(f) exp(2\pi i f t) df \tag{2.6}$$

In addition, the convolution theorem asserts that a convolution in the time domain is equivalent to a multiplication in the Fourier domain. Mathematically, when we convolve a function $h(t)$ with another function $g(t)$, we obtain a multiplication of the spectra of $h(t)$ and $g(t)$.

$$F_t(\int_{-\infty}^{+\infty} h(t')g(t-t')dt') = H(f)G(f) \tag{2.7}$$

where F_t denotes the Fourier transform with respect to the subscript variable t. A convolution in the Fourier domain is analogous to a multiplication in the time domain. We will make frequent use of this property.

In seismic processing, the Fourier transform, specifically the Fast Fourier Transform (FFT), is applied to seismic traces, which are time-recorded measurements of ground motion. A seismic trace is decomposed by the Fourier transform into a series of sinusoidal components, each with its own frequency and amplitude. This representation in the frequency domain provides valuable insights into the seismic data and permits the performance of specific operations.

By employing the Fourier transform in seismic processing, geophysicists are able to extract valuable information from seismic data, improve the quality and interpretability of the data, and enhance their imaging and comprehension of subsurface structures. It is a versatile instrument that is widely employed throughout the various processing and interpretation stages of seismic data.

2.1.3.2 Finite difference modeling

In geophysics and seismic exploration, finite difference modeling is a popular numerical technique for simulating wave propagation through the subsurface. It requires discretizing the governing wave equation into a set of finite difference equations that can be iteratively solved on a computational grid.

Using a grid of points, the finite difference method approximates the spatial and temporal derivatives of the wave equation. At each grid point, the values of the wavefield variables (such as pressure or particle velocity) are calculated. The wave equation is then discretized at each grid point using finite difference approximations, resulting in a numerically solvable system of equations.

For simplicity the 2-D acoustic wave equation with a source term (s(t)) [6].

$$\frac{\partial^2 P}{\partial x^2} + \frac{\partial^2 P}{\partial z^2} = \frac{1}{c^2}\frac{\partial^2 P}{\partial t^2} + s(t)\delta(x - x_s)\delta(z - z_s) \tag{2.8}$$

We discretize in both time and space in order to solve the above equation.

$$t = n\Delta t \tag{2.9}$$

$$x = i\Delta x \tag{2.10}$$

$$z = j\Delta z \tag{2.11}$$

A Taylor series expansion of the second pressure derivative with respect to time yields the result.

$$\frac{\partial^2 P}{\partial t^2} \cong \frac{P^{n+1} - 2P^n + P^{n-1}}{(\Delta t)^2} \tag{2.12}$$

Where $P^n + 1 = P((n + 1)\Delta t)$. If we choose to use a second order Taylor expansion for evaluating the spatial derivatives we obtain

$$\frac{\partial^2 P}{\partial x^2} \cong \frac{P^n(i + 1, j) - 2P^n(i, j) + P^n(i - 1, j)}{(\Delta x)^2} \tag{2.13}$$

for spatial differentiation in the x-direction, and similarly for the z-direction

$$\frac{\partial^2 P}{\partial z^2} \cong \frac{P^n(i, j + 1) - 2P^n(i, j) + P^n(i, j - 1)}{(\Delta z)^2} \tag{2.14}$$

Using these approximations, it is now possible to write the wave equation.

$$\begin{aligned} P^{n+1}(i, j) = 2P^n - P^{n-1} + (c(i, j)\Delta t)^2\{&\tfrac{P^n(i+1,j) - 2P^n(i,j) + P^n(i-1,j)}{(\Delta x)^2} \\ &+ \tfrac{P^n(i,j+1) - 2P^n(i,j) + P^n(i,j-1)}{(\Delta z)^2} - s^n(i, j)\} \end{aligned} \tag{2.15}$$

Given the source time function (s(t)) and its location (x_s, z_s), and the boundary conditions can be solved if the velocity field $(c(imj))$ also is known. As an example of boundary conditions, the pressure at the free surface could be zero.

$$P(x, z = 0, t) = 0 \tag{2.16}$$

and for time less than zero, the pressure is zero. When a seismic wave collides with the edge of a finite difference grid, the wave will be reflected back into the grid, resulting in undesirable artifacts. In order to circumvent this issue, absorbers are frequently placed around the finite difference model grid (though not at the free surface, as reflections from the free surface are part of a real seismic experiment and should therefore be modeled). The effect of these absorbing layers surrounding the model is to reduce the seismic energy so that the amplitude of the waves reflected at the edge of the finite difference grid is practically zero. Grid dispersion is another issue to be aware of when using finite difference modeling. Dispersion indicates that the phase speed of a wave is a function of its frequency, such that high frequencies travel faster than low frequencies, for instance. For the analysis of temporal dispersion, a one-dimensional wave equation can be utilized [6].

$$\frac{\partial^2 P}{\partial t^2} = {c_0}^2 \frac{\partial^2 P}{\partial x^2} \tag{2.17}$$

and introducing an harmonic pressure solution

$$P \sim e^{i(\omega t - kx)} \tag{2.18}$$

into one-dimensional wave equation yields

$$\omega^2 = {c_0}^2 k^2 \tag{2.19}$$

which means that the phase speed ($\frac{\omega}{k}$) equals the velocity of sound. However, when we use a solution based on finite differences, we can solve the equation.

$$\frac{P^{n+1} - 2P^n + P^{n-1}}{(\Delta t)^2} = {c_0}^2 \frac{\partial^2 P}{\partial x^2} \tag{2.20}$$

and insert harmonic solution we get

$$\frac{1}{(\Delta t)^2}[e^{i\omega\Delta t} - 2 + e^{-i\omega\Delta t}] = -{c_0}^2 k^2 \tag{2.21}$$

The phase speed is equal to $\frac{\omega}{k}$, and after Taylor expansion of the left side of this side of this equation we get

$$\frac{c^2}{c_0^2} = 1 + \frac{(\omega\Delta t)^2}{12} \tag{2.22}$$

Consequently, high frequencies travel faster than low frequencies, and the amount of temporal grid dispersion is proportional to the square of the time step used for modeling. Similarly, we can demonstrate the dispersion of the spatial grid.

$$\frac{c^2}{c_0^2} = 1 - \frac{(k\Delta t)^2}{12} \tag{2.23}$$

Due to the fact that a computer uses a limited number of digits to represent a given number, there is always a risk of instability resulting from such inaccuracies which is referred to as the Courant number. To prevent numerical instability, one must ensure that the ratio between temporal and spatial sampling is constrained. For the 2nd order scheme discussed here, it can be demonstrated that this ratio should be chosen.

$$\frac{c\Delta t}{\Delta x} \leq \frac{1}{\sqrt{2}} \tag{2.24}$$

Finally, one should be aware that the number of grid points per shortest wavelength decreases as the wavelength decreases. Fine grid methods typically use 20 gridpoints per shortest wavelength, while coarse grid methods (using higher order differential operators) can only use 4-5 gridpoints.

CHAPTER

THREE

GEOLOGICAL BACKGROUND

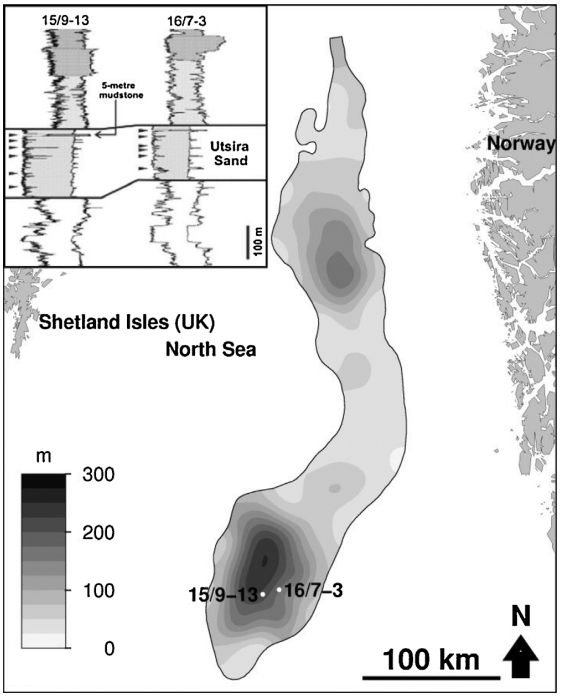

Figure 3.0.1: Isopach map of the Utsira Sand and representative geophysical well logs showing reservoir heterogeneity [5].

This thesis is motivated by the uppermost layer of Sleipner field. The carbon dioxide extracted from the natural gas produced at the Sleipner field in the North Sea (Norwegian block 15/9) is injected into the Utsira Sand, a regional saline aquifer dating back to the late Cenozoic (Figure 3.0.1). The Utsira sand has a complex tectonic history, including multiple phases of faulting and uplifting which have contributed to the formation and preservation of hydrocarbon traps in the area. With a maximum thickness of over 300 meters, the Utsira sandstone lies beneath 800–1000 meters of sediment beneath the sea, as determined by 3D seismic data [9]. The Utsira stretches north to south for 450 kilometers and east to west for 90 kilometers [10]. In the north and south, there are deep sand systems, whereas in the middle region, the seafloor is covered by thinner deposits. In the Sleipner region, the aquifer is typically thicker than 200 meters and is almost entirely

composed of unconsolidated sand with a high porosity ($> 30\%$) and permeability (> 1 Darcy) [5]. At a depth of approximately 1012 meters below sea level and 200 meters below the aquifer's top, carbon dioxide is injected in dense phase via a deviated well.

CHAPTER

FOUR

RESULTS

To use one acquisition geometry on CO2 detection, three scenarios were considered: absence of a CO2 layer, CO2 layer at true depth, and CO2 layer at shallower depth. Each scenario was simulated using seismic modeling techniques to analyze the resulting seismic data.

4.1 Velocity model

A velocity model was constructed to represent the subsurface for the seismic simulations. The velocity models are inspired by Sleipner field sharing the same depth for the top CO2 layer and based on Without CO2 layer scenario. The velocity model provided the necessary information about the speed at which seismic waves propagate through different geological layers.

Parameter	True depth	Shallower depth	No thin layer
P-wave velocity in the water	1500 m/s	1500 m/s	1500 m/s
P-wave velocity at seabed	1714 m/s	1714 m/s	1714 m/s
Velocity gradient	$0.5s^-1$	$0.5s^-1$	$0.5s^-1$
Depth of water column	70 m	70 m	70 m
Density	1000 kg/m^3	1000 kg/m^3	1000 kg/m^3
Top depth of the CO2 layer	800 m	400 m	-
CO2 layer length	3000 m	3000 m	-
CO2 layer velocity	1700 m/s	1600 m/s	-
CO2 layer thickness	50 m	50 m	-
Left Edge of CO2 layer	11500 m	11500 m	-

Table 4.1.1: Velocity model parameters for three scenarios

Various parameters were considered in the construction of the velocity model, including P-wave, density, grid size, etc. Specifically, density is homogeneous. In this model, acoustic wave equation was applied and that is why S-wave is not used. The velocity model played a role in simply simulating the seismic wave propagation and reflection behavior which only captures the reflection from the top and base of the CO2 layer and seabed in each scenario.

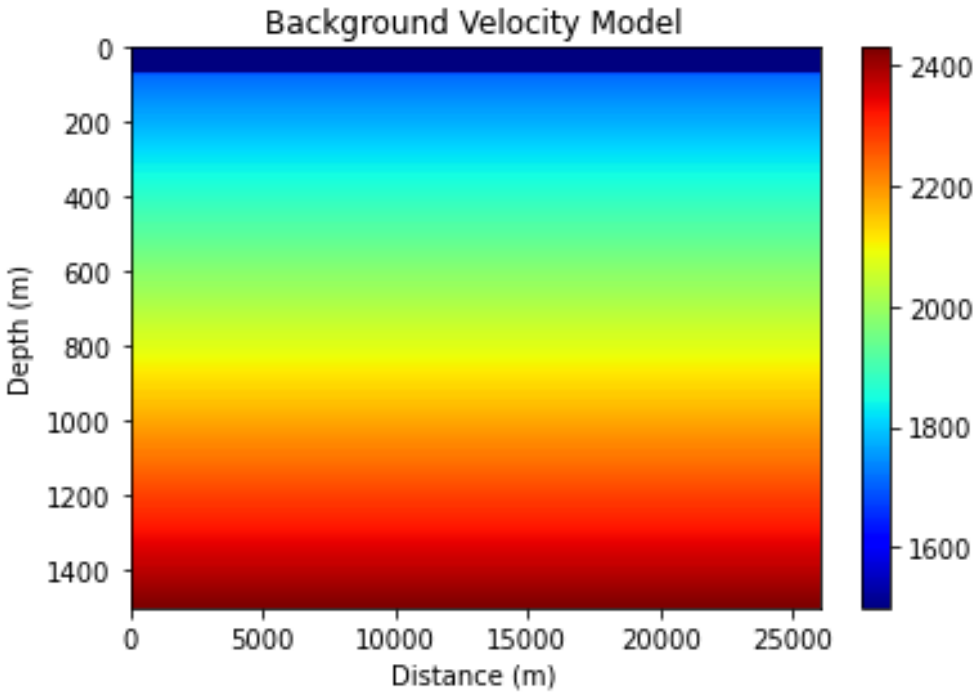

Figure 4.1.1: Velocity model of without CO2 layer.

Before CO2 injection, this model is essential for establishing a baseline understanding of the subsurface's structure and properties. It reflects the natural geological formations and fluid compositions devoid of injected CO2. This model's purpose is to serve as a standard against which subsequent velocity models can be compared. It aids in identifying and differentiating the changes in velocity and seismic response brought on by the presence of CO2.

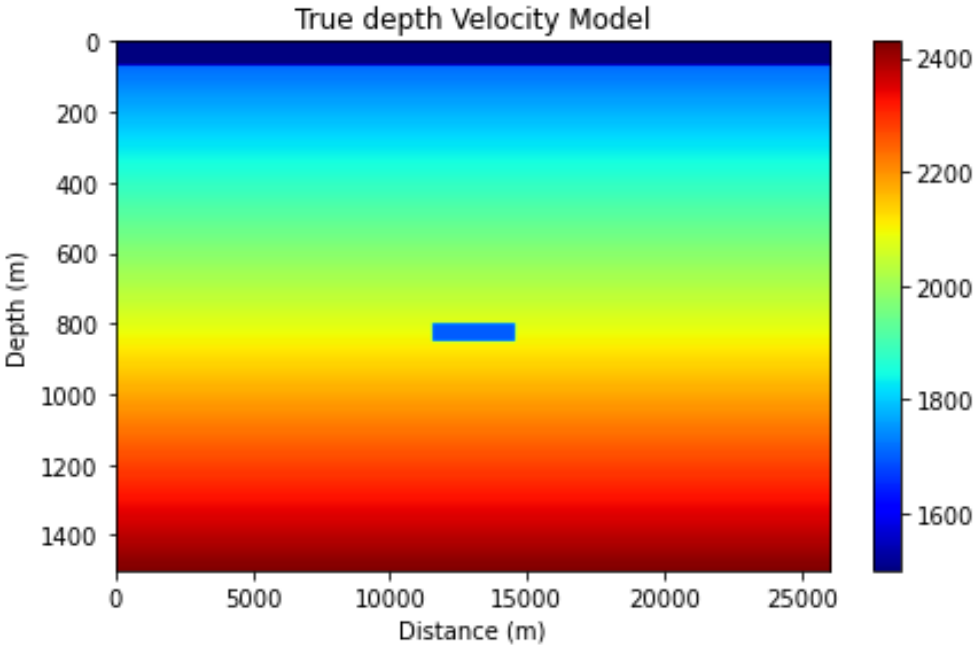

Figure 4.1.2: Velocity model of true depth CO2 layer.

The CO2 layer at the true depth as 800 m velocity model represents a scenario where CO2 has been injected into the subsurface and has accumulated at its intended depth. It provides insights into the seismic response and velocity changes associated with the CO2 accumulation.

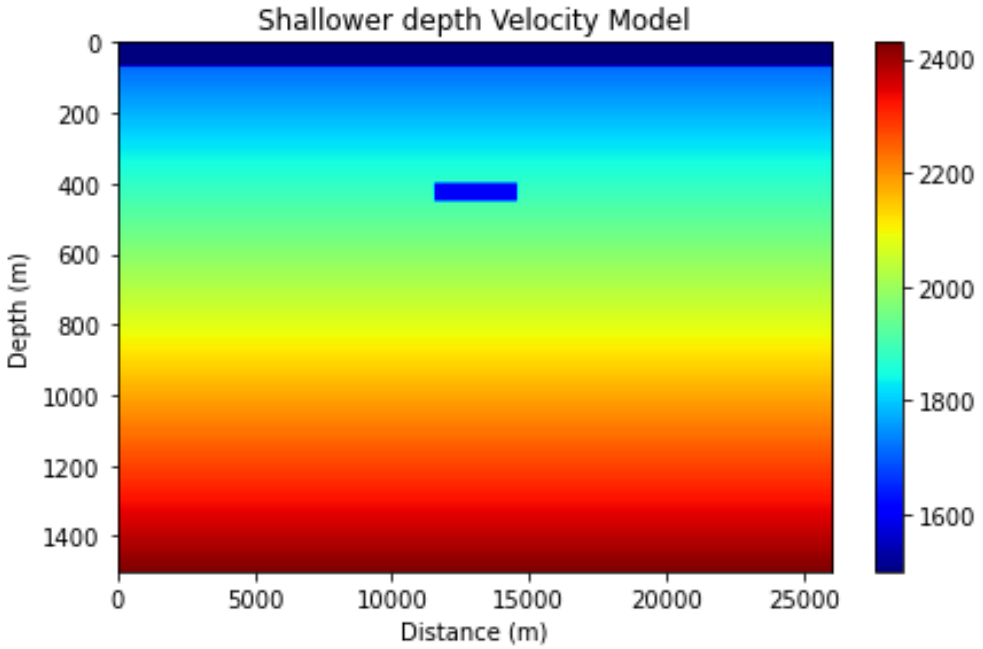

Figure 4.1.3: Velocity model of shallower depth CO2 layer.

The CO2 layer at shallower depth velocity model represents a scenario where CO2 leakage or migration has occurred from its intended storage depth to a shallower position. It helps in understanding the challenges associated with monitoring and mitigating CO2 leaks.

4.2 Geometry

Parameter	Values
Number of samples	7501
Time Step	1 ms
Shot Interval	200 m
Receiver Interval	20 m
Number of sources to use	33
Maximum Offset	6000 m
Source Depth	10 m
Receiver Depth	10 m
Position of first source	8300 m
Position of last source	14700 m
Wavelet Peak Frequency	20 Hz

Table 4.2.1: Geometry parameters

Using geometry parameters, the layout and arrangement of seismic sources and receivers were determined [2]. These parameters determine the spatial configuration of the acquisition, which impacts the quality and efficacy of the acquired data.

4.2.1 Wavelet

A suitable wavelet was chosen to represent the seismic source signature for the simulations. The wavelet acted as the input signal that generated the seismic waves in the modeled scenarios. Its characteristics, such as frequency content and amplitude, were carefully selected to mimic real-world seismic sources.

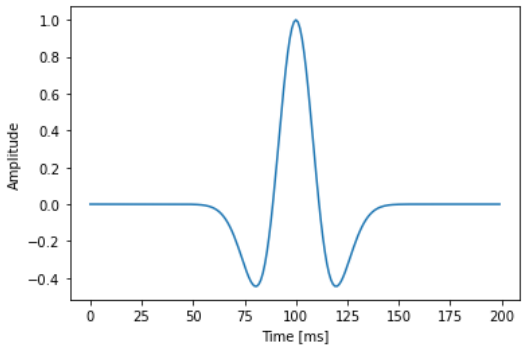

(a) Ricker wavelet

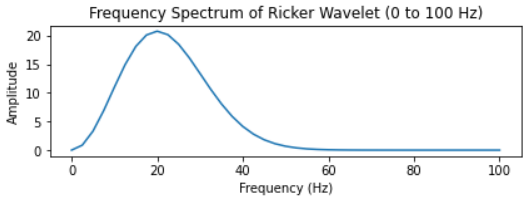

(b) Frequency spectrum

Figure 4.2.1: Dominant frequency as 20Hz

The Ricker wavelet is used as a common wavelet for wavelet analysis. In the case of the Ricker wavelet, the spectrum reveals its dominant frequency, which corresponds to the central frequency of the wavelet as 20Hz. It is slightly lower than the 30-50Hz average peak frequency in seismic surveys. It serve as a basis for comparison with the output seismic data to determine the similarity of dissimilarity between them.

4.2.2 Source and Receiver

Source and receiver locations were specified based on the acquisition configuration for each scenario. The positions of seismic sources and receivers were strategically chosen to optimize data coverage and capture relevant seismic information. It is simulated by single gun with following receivers. The first receiver located at the same location of source as zero offset. Shot gathers and common-offset displays were also generated to facilitate further analysis and processing.

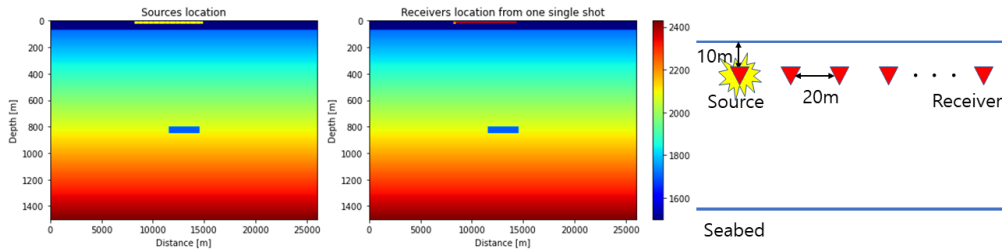

Figure 4.2.2: Source and Receivers location.

4.2.3 Model execution and Runtime feasibility analysis

The seismic modeling was performed using appropriate numerical solvers and computational software which is called Skald. The selected modeling software implemented finite difference algorithms to solve the wave equation numerically on the computational grid.

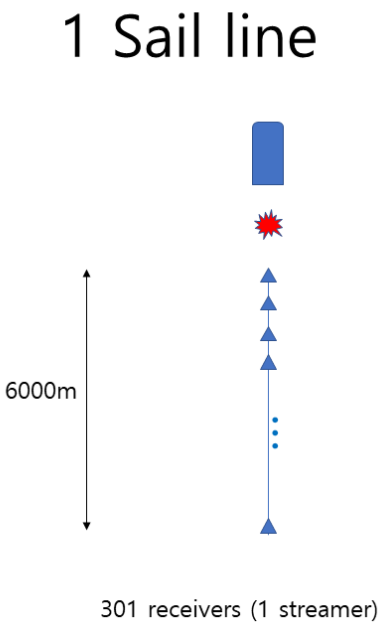

Figure 4.2.3: Seismic data acquisition in one sail line.

The simulations were executed with the defined velocity model, wavelet, and source/receiver configurations. The runtime of the simulations was recorded to assess the computational requirements and efficiency of the modeling process.

Run time for the modelling is important. The run times are closely related to how to define the problem. For examaple, grid sizes in the modelling, sampling interval and the length of our records. These depend on the geological event of interest and the type of geological features, such as a thin layer of CO2 requiring a finer grid size than a thick channel or tunnel valley. In adiition, the finer the grid size the longer the run times. Based on the run time of one single shot of each scenario, all shots run time were computed with multiplying of the number of shots 33.

Runtime	One single shot	1 sailine with 33 shots
CO2 at true depth	106 min	3498 min
CO2 at shallower depth	70 min	2310 min
No thin layer	69 min	2277 min

Table 4.2.2: Initial modelling runtime

After run the model, the runtime was way longer than I expected. To make runtime smaller, I need to try to put different values of parameters.

- Use smaller model - decrease nx, nz grid points
- Coarser grid size - change dz
- Use another different nt (time step)
- Decrease Interpolation radius - can make result inprecisely

Changing grid size dz to 10 and spatial sampling dx to 100 is anticipated to take under 10 seconds. However, it did not work quickly enough on my machine. A computer glitch was the cause of the lengthy duration. Due to the fact that the computer used to run the model is a shared machine and another user was running his own model. As a result, my order was placed behind his, and I had to wait in a lengthy line. By entering specific commands for running the model, the issue was able to be resolved. (appendix)

Runtime	One single shot	1 sailine with 33 shots
CO2 at true depth	493 s	16269 s
CO2 at shallower depth	365 s	12045 s
No thin layer	93 s	3069 s

Table 4.2.3: Final modelling runtime

Parameter	dz	nx	ny	nt	dt
CO2 at true depth	2	2601	751	7501	0.001
CO2 at shallower depth	2	2601	751	7501	0.001
No thin layer	10	2601	151	7501	0.001

Table 4.2.4: Parameters for the model

4.3 Shot gather analysis

After simulation, the output data were analyzed in SEG-Y format to extract shot gathers for further analysis. Shot gathers are the seismic data recorded at each receiver location for a given source location. The free surface functions as a reflective boundary for the simulation's seismic waves. Due to a number of factors, the free surface produces multiple and ghost reflections.

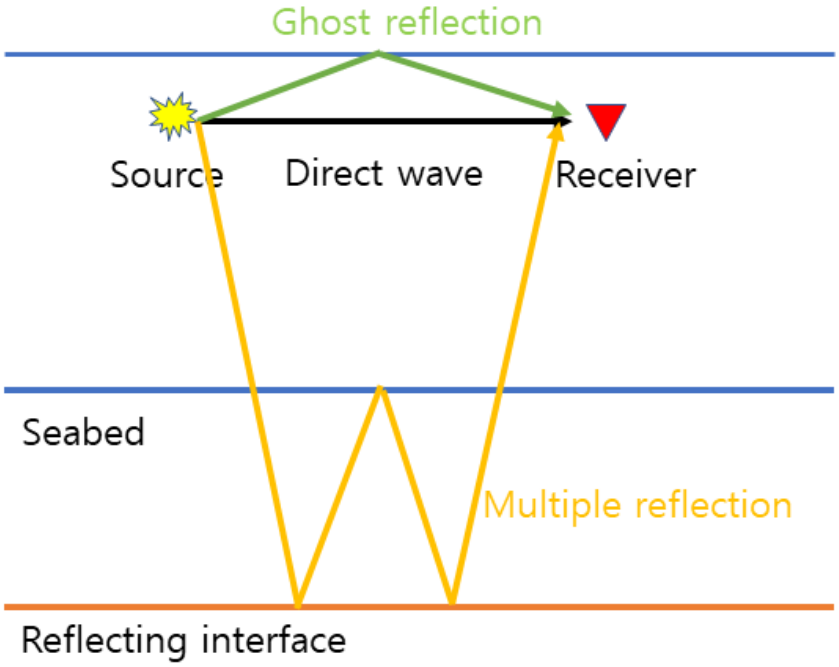

Figure 4.3.1: Multiple reflection and ghost reflection.

Multiple reflections occur when seismic waves reflect multiple times between various subsurface interfaces prior to reaching receivers. Each reflection represents a unique subsurface interface[4].

Ghost reflections are caused by irregularities or impedance variations in the near-surface or shallow subsurface. These irregularities can result in partial energy scattering or refraction, leading to the appearance of additional, weaker reflections alongside the primary reflection. In shallow or complex geological environments, ghost reflections can interfere with the primary reflection and make interpretation more difficult[9][11].

4.3.1 No CO2 layer model

No CO2 layer scenario is assuming before injecting the CO2 to subsurface.

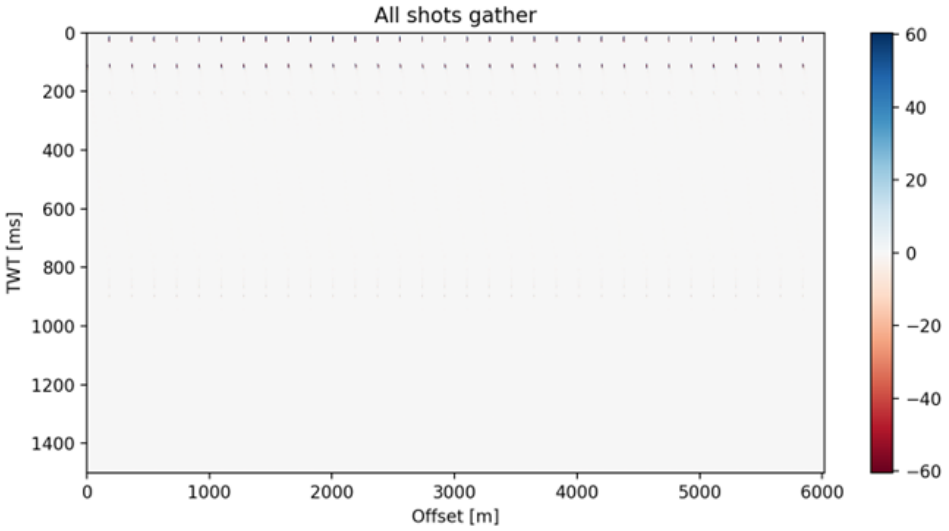

Figure 4.3.2: All shots gather of without CO2 layer.

From the all shots gather, there are reflections at the top. Also, around 100 ms we can see the seabed. There are no reflection under the seabed which means no geological formation under the seabed in this scenario.

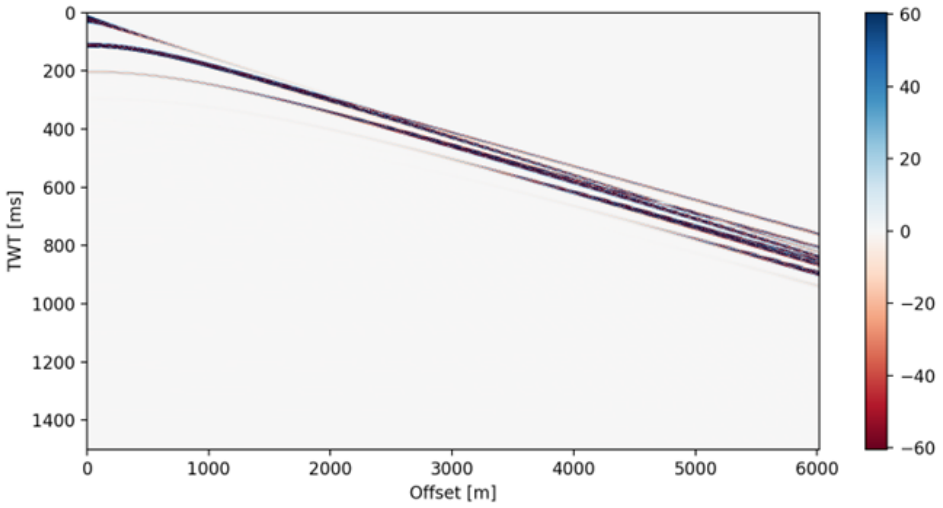

Figure 4.3.3: Picked 24th shot from no thin layer model.

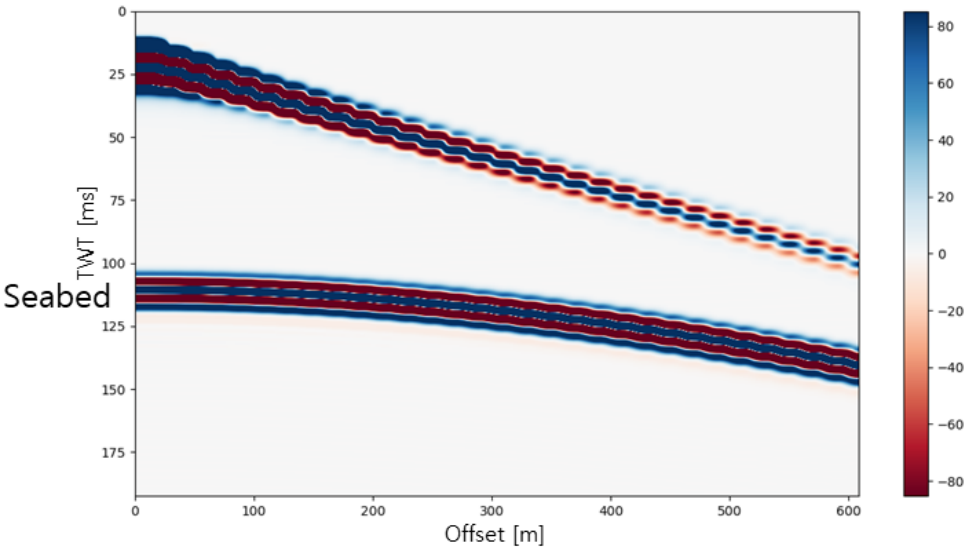

Figure 4.3.4: Zoom in seabed flection.

To check whether the output data and set up parameters match or not, comparing amplitude differences and travel time differences needed. There is delayed shot time for 10 ms and the water column depth is 70 m. The velocity of water column is 1500 m/s and the two way travel time of seabed is 102 ms. Since it is two way travel, it should be divided by 2 and subtract 10 ms to the TWT of seabed because of the delayed shot time 10 ms. From zoom in figure 4.3.4, the reflection is determined as a seabed.

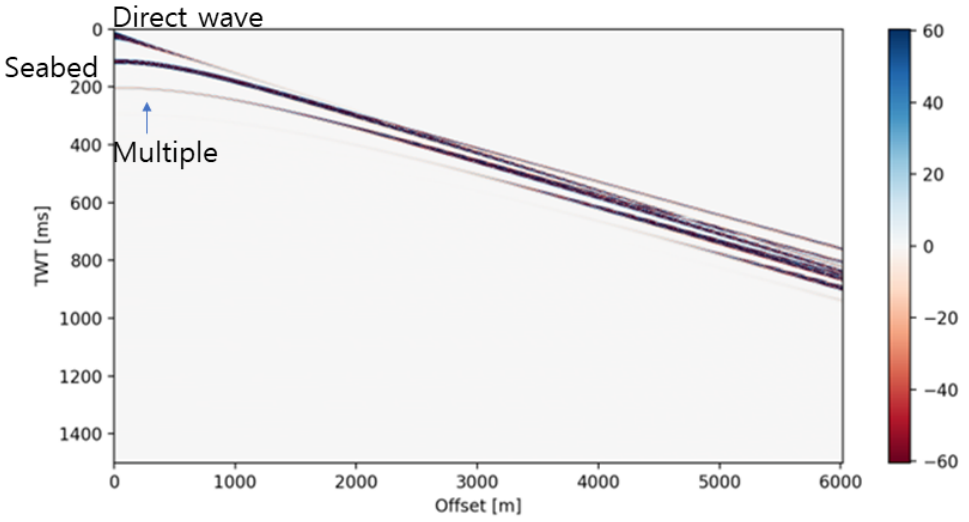

Figure 4.3.5: Interpretation of the no thin layer scenario.

Integrating all the interpretation, figure 4.3.5 is the result of the 24th shot of no thin layer scenario. Only direct wave, seabed and multiples are shown.

4.3.2 CO2 layer at true depth model

True depth CO2 layer scenario is assuming after injecting the CO2 to 800 m depth.

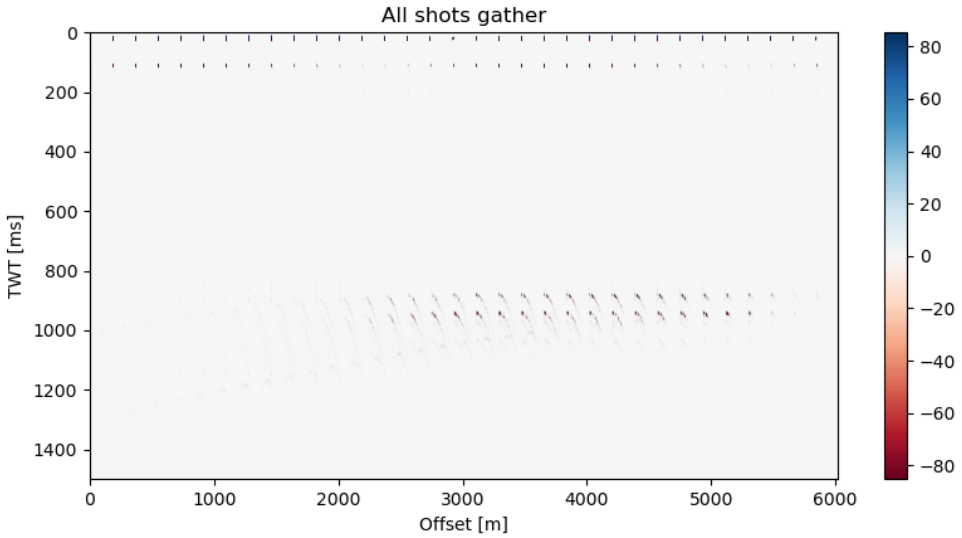

Figure 4.3.6: All shots gather of true depth CO2 layer.

There are reflections at the top of all shots gather and a seabed TWT is approximately 100 ms. Around 800 ms to 1000 ms, the reflection of the CO2 layer is observed. However, there are no reflections below the left edge. To examine in detail, the 24th shot from this shots gather was chosen.

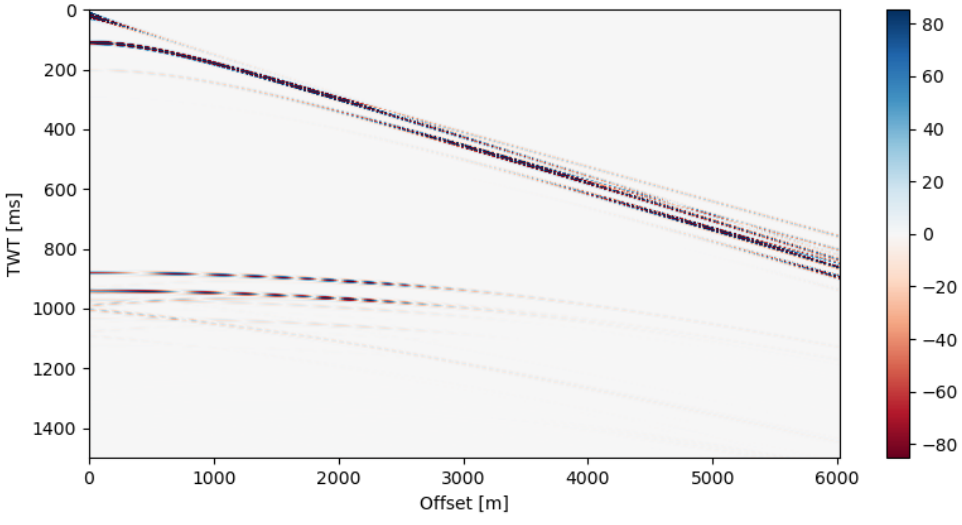

Figure 4.3.7: Picked 24th shot from true depth model.

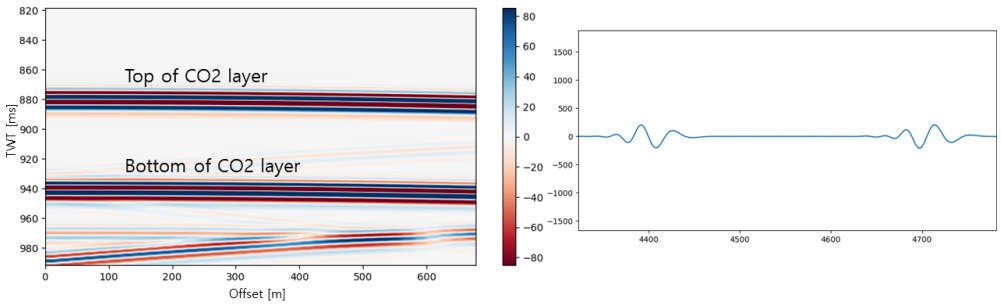

Figure 4.3.8: Zoom in CO2 layer.

The TWT at the top of CO2 layer is 880 ms, and the average velocity of overburden layer is 1800 m/s. The formation has a depth of 792 meters, which is very close to the depth of the top of the CO2 layer. The depth of CO2 layer in true depth model is 800 m. To ensure that the lower formation is the base of the CO2 layer, we can also compute from TWT. The thickness of the CO2 layer is 50 m, so the distance between the top and bottom of the layer should be 60 ms, as depicted in the figure 4.3.8. Also, the polarity should be reversed when it propagates from the CO2 layer. The top of the CO2 layer is negative and the bottom is positive.

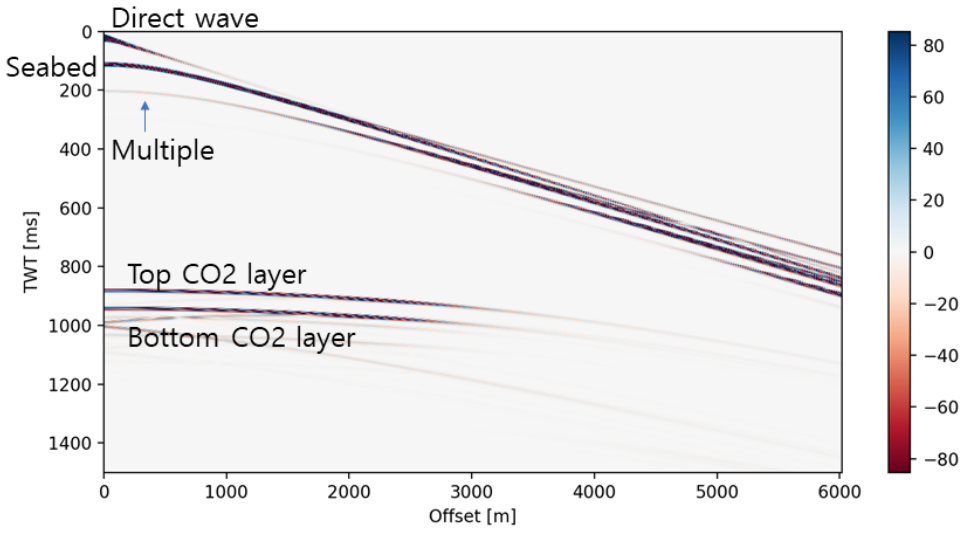

Figure 4.3.9: Interpretation of the seismogram.

Integrating all the interpretation, figure 4.3.9 is the result. Direct wave, seabed, multiple, top of CO2 layer, and Bottom of CO2 layer is shown.

Shot gathers were processed to determine the near, far, and very far offsets, which correspond to various source-to-receiver distances. To define near, far, and very far offset sections, the critical angle and critical offset should be applied. Based on equation 2.4 and the velocity model (4.1.2, the critical angle in this scenario is 54 degrees. (appendix)

$$critical\ offset = \frac{depth}{tan(critical\ angle)} \tag{4.1}$$

Critical angle is 54 from the velocity model (figure 4.1.2. The critical offset is 754.8 meters based on the critical offset equation, which is 800 meters divided by 54. To compare the various images, I need to display the extracted traces at their respective midpoints.

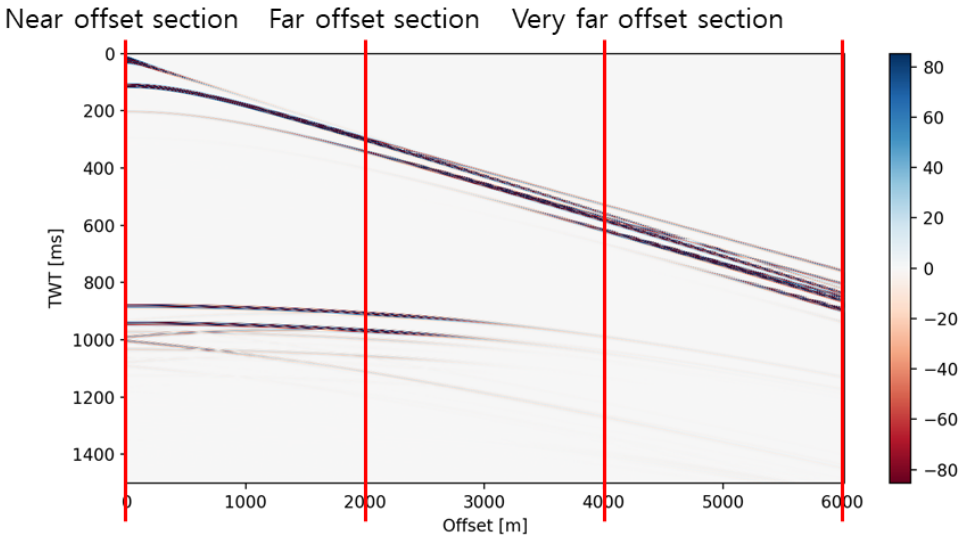

Figure 4.3.10: Near, far, very far offset section.

Near offsets capture information from shallow subsurface layers, far offsets provide an intermediate view, and very far offsets as a transmission section provide information from deeper layers.

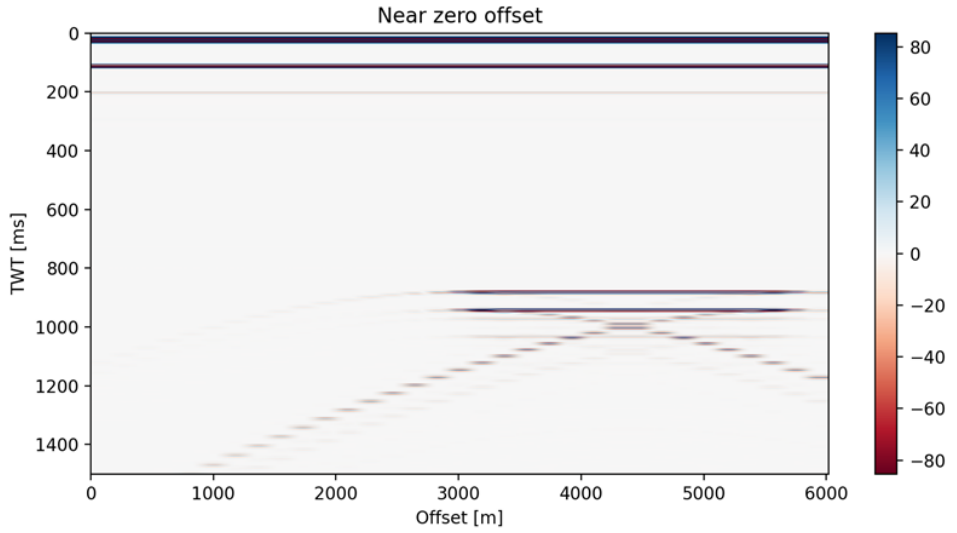

Figure 4.3.11: Near zero offset section of true depth scenario.

Reflections from near-offset shot gathers tend to be stronger and exhibit higher resolution due to the proximity to the source and shallow subsurface reflections. For a near offset section, the trace recorded at the first receiver with an offset of 0 was selected and extracted this trace for each shot.

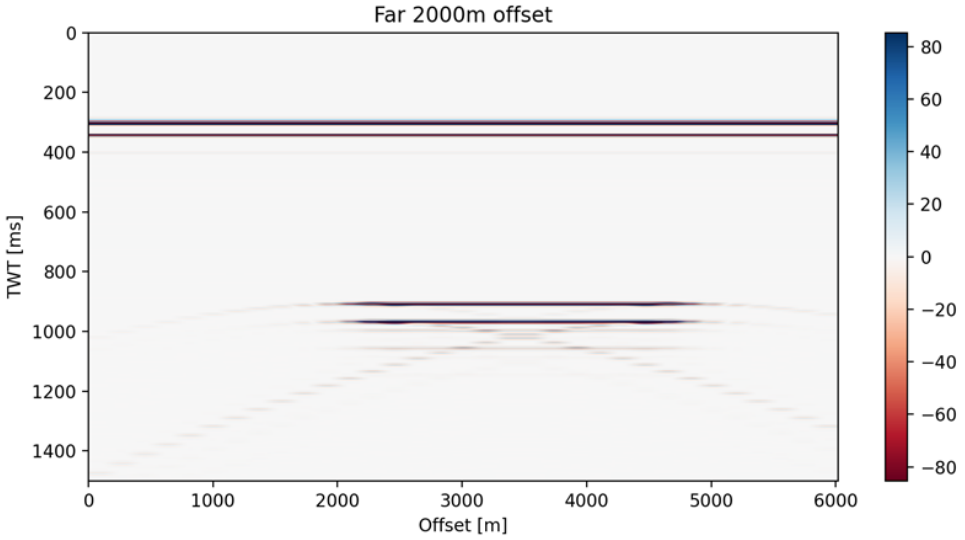

Figure 4.3.12: Far offset section as 2000 m offset.

Far offset shot gathers capture a balance between shallow and deeper subsurface reflections. Analyze the variations in reflection amplitudes and continuity to identify potential pathways that extend to intermediate depths.

For a far offset section, an offset or receiver before reaching the critical reflection angle or critical offset was chosen.

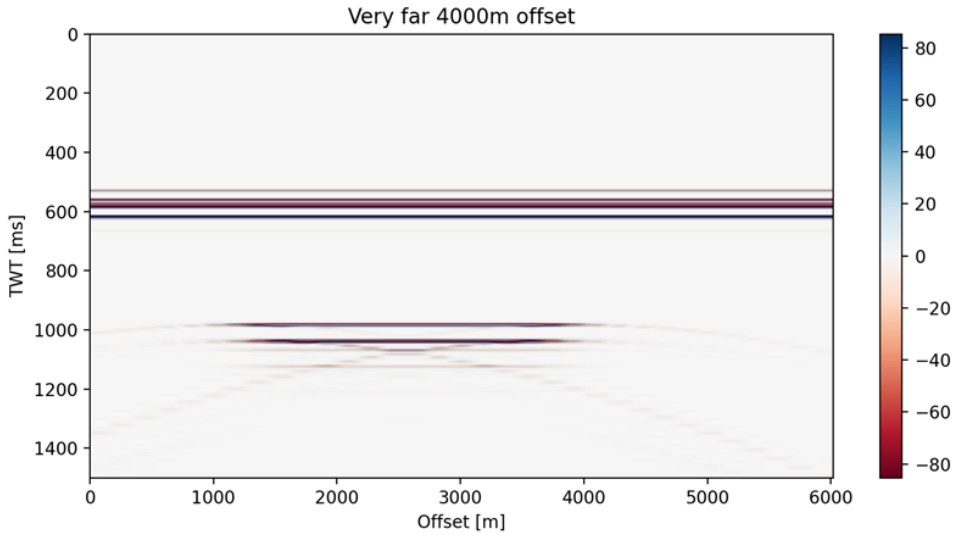

Figure 4.3.13: Very far offset section as 4000 m offset.

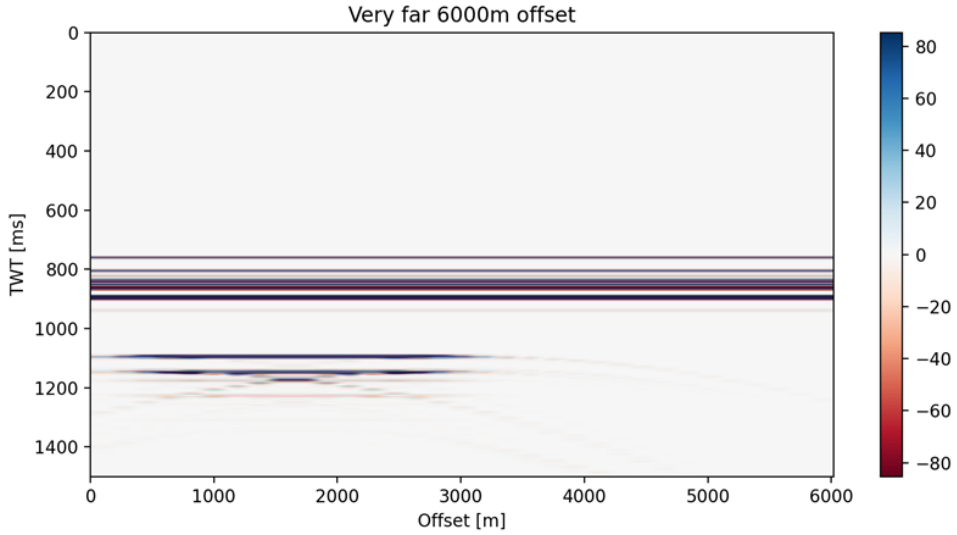

Figure 4.3.14: Very far offset section as 6000 m offset.

Far-offset shot gathers provide insights into deeper subsurface structures. Analyze the reflections to identify potential migration pathways at greater depths. For very far offset as transmissions, a very far receiver, generally in the post-critical region was chosen.

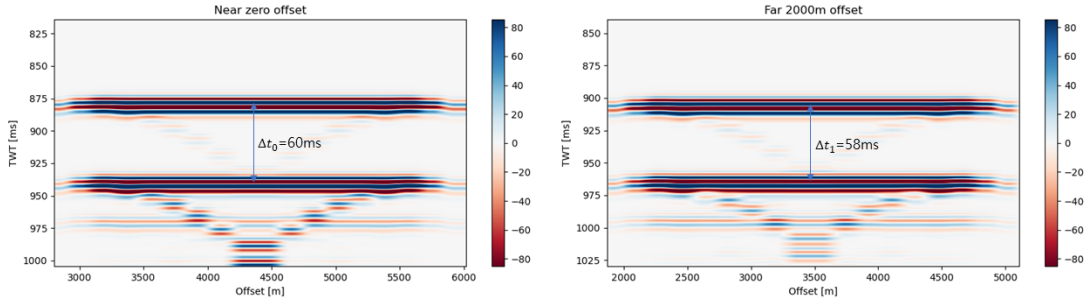

Figure 4.3.15: CO2 layer TWT difference between near and far offset.

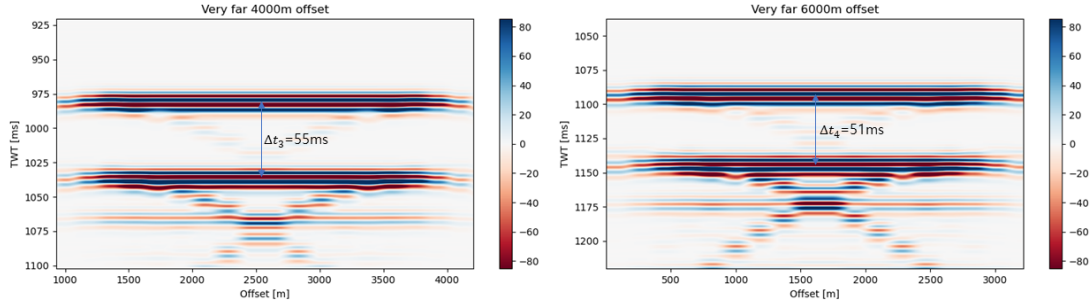

Figure 4.3.16: CO2 layer TWT difference between very far offsets.

In case of my near, far, very far offset sections, they showed the TWT from top to bottom of CO2 layer getting decreased.

4.3.3 CO2 layer at shallower depth model

Shallower depth CO2 layer scenario is assuming after injecting the CO2 to 800 m depth, the CO2 leaked or migrated to the shallower depth which is 400m.

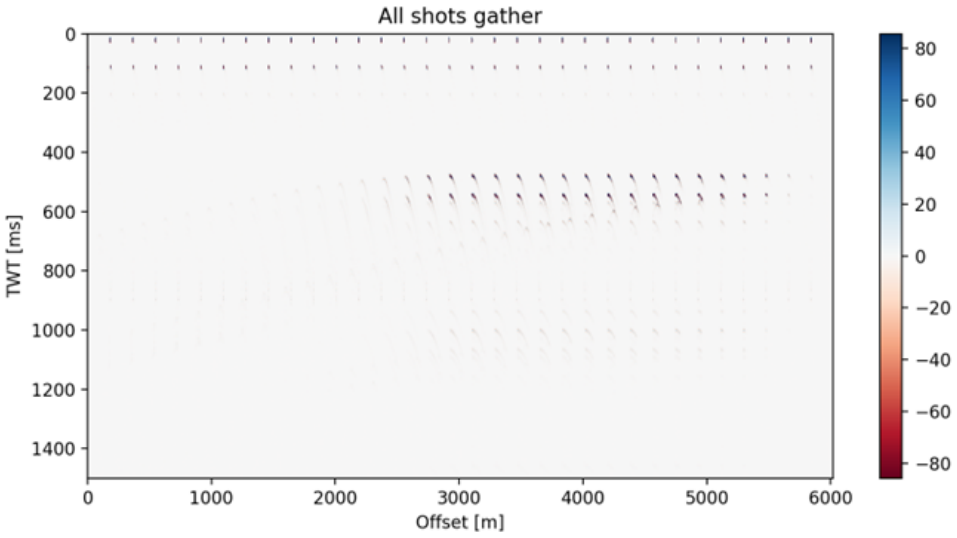

Figure 4.3.17: All shots gather of shallower depth CO2 layer.

From the all shots gather, there are reflections at the top and around 100 ms, sea bed is observed. Around 400 to 600, a CO2 layer reflection is seen. But there are no reflections at the left below edge. To look in detail, the 24th shot of this shot gather was picked.

Shallower depth model mostly follows true depth model. There are reflections at the top of all shots gather, and the seabed from a distance of approximately 100 ms is observed as same as true depth model. Around 400 ms to 600 ms, the reflection of the CO2 layer is observed. However, there are no reflections below the left edge. To examine in detail and compare with true depth model, the same number of 24th shot from this shots gather was selected.

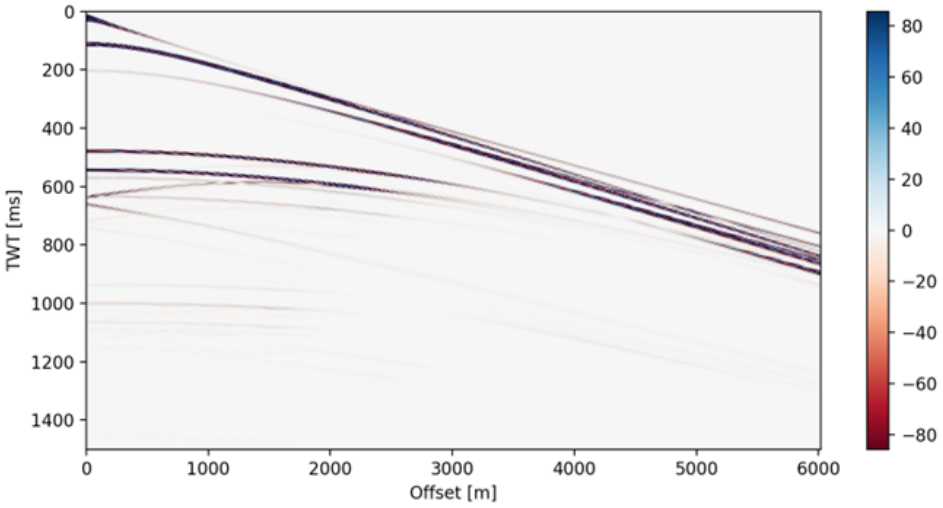

Figure 4.3.18: Picked 24th shot from shallower depth model.

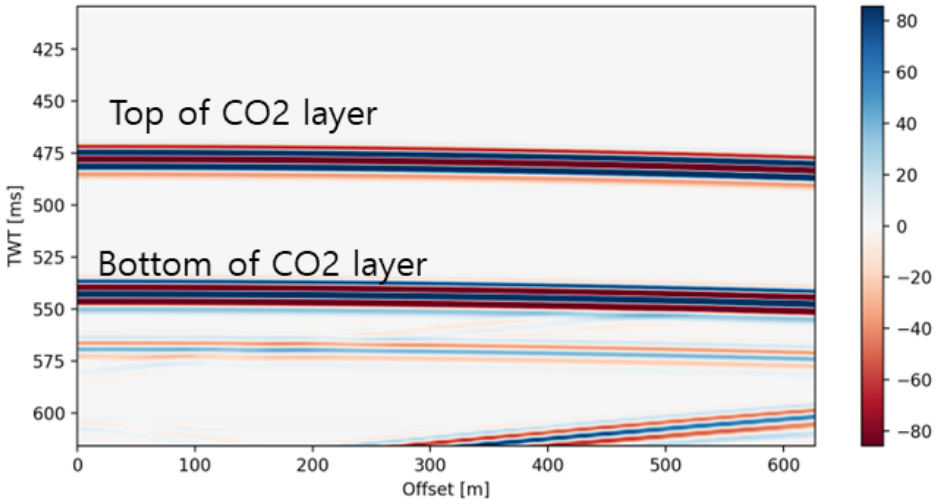

Figure 4.3.19: Zoom in CO2 layer.

The TWT at the top of CO2 layer is 475 ms, and the average velocity of overburden layer is 1700 m/s. The formation has a depth of 403 meters, which is very close to the depth of the top of the CO2 layer. The depth of CO2 layer in shallower depth model is 400 m. Computing TWT can ensure the lower formation as a base of the CO2 layer. The thickness of the CO2 layer is 50 m, so the distance between the top and bottom of the layer should be 60 ms, as depicted in the figure 4.3.19. Also, the polarity should be reversed when it propagates from the CO2 layer. The top of the CO2 layer is negative and the bottom is positive as same as true depth model.

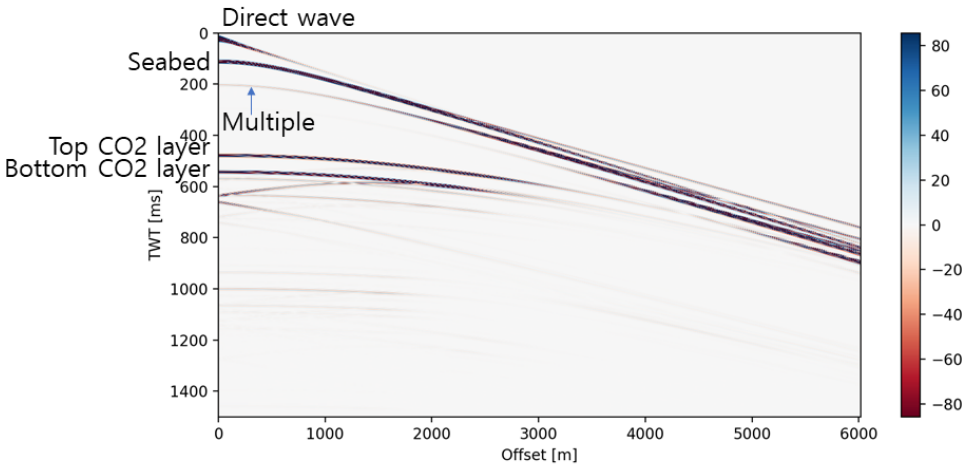

Figure 4.3.20: Interpretation of the seismogram.

Integrating all the interpretation, figure 4.3.20 is the result. Direct wave, seabed, multiples, top and bottom of CO2 layer are shown but with different depth of CO2 layer.

Critical angle is 57 from the velocity model (figure 4.1.3. The critical offset is 754.8 meters based on the critical offset equation, which is 400 meters divided by 57.

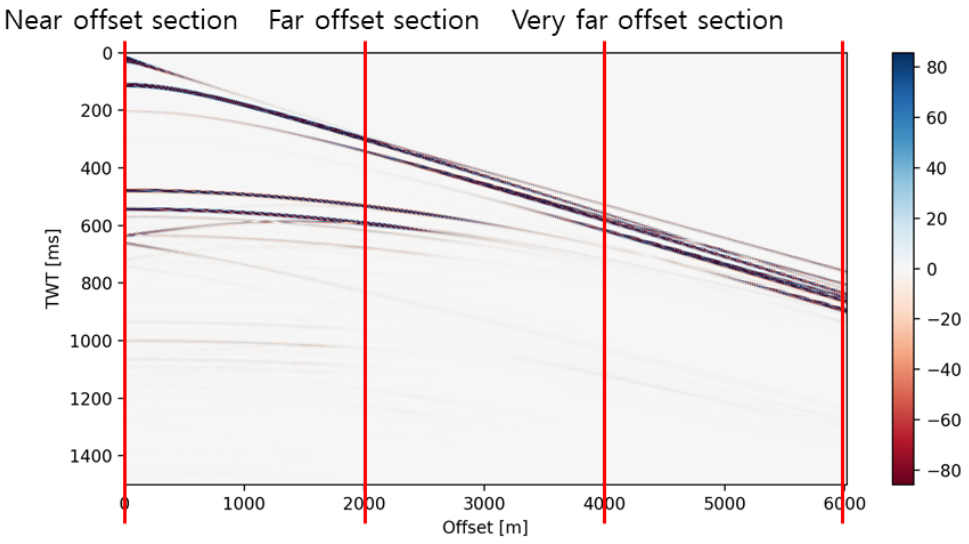

Figure 4.3.21: Near, far, very far offset section.

Following steps would be same as true depth model.

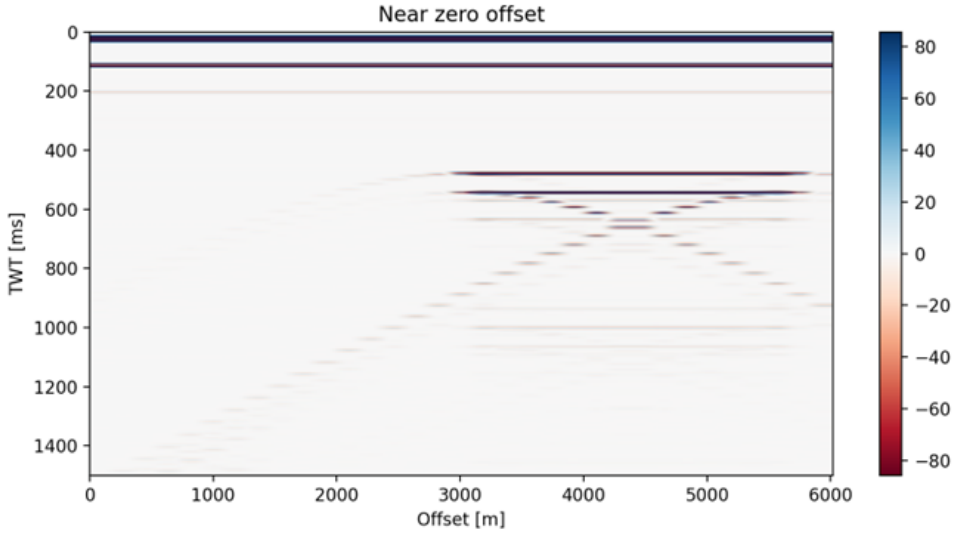

Figure 4.3.22: Near zero offset section of shallower depth scenario.

For a near offset section, zero offset which is first receiver among 301 was chosen to compare with true depth model in same environment.

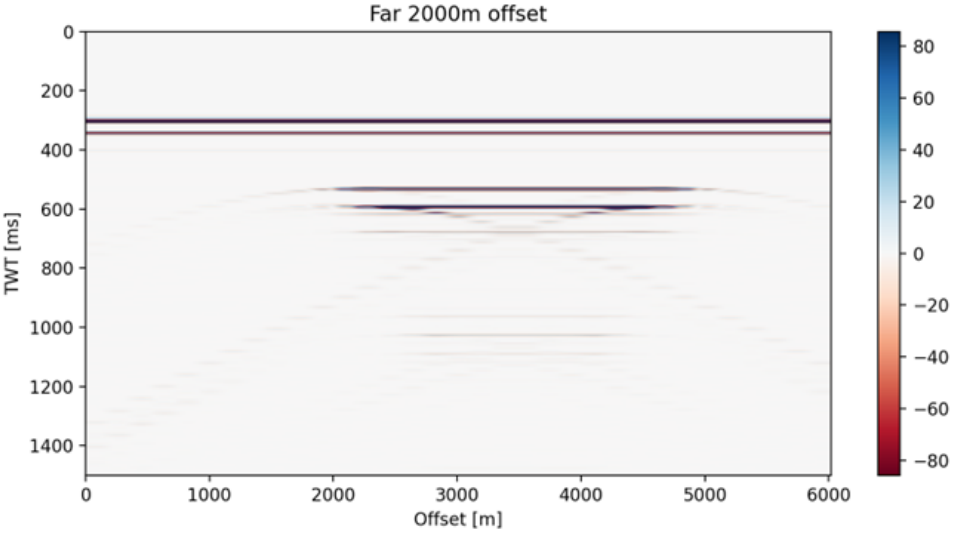

Figure 4.3.23: Far offset section as 2000 m offset.

For a far offset section, 2000m offset was chosen.

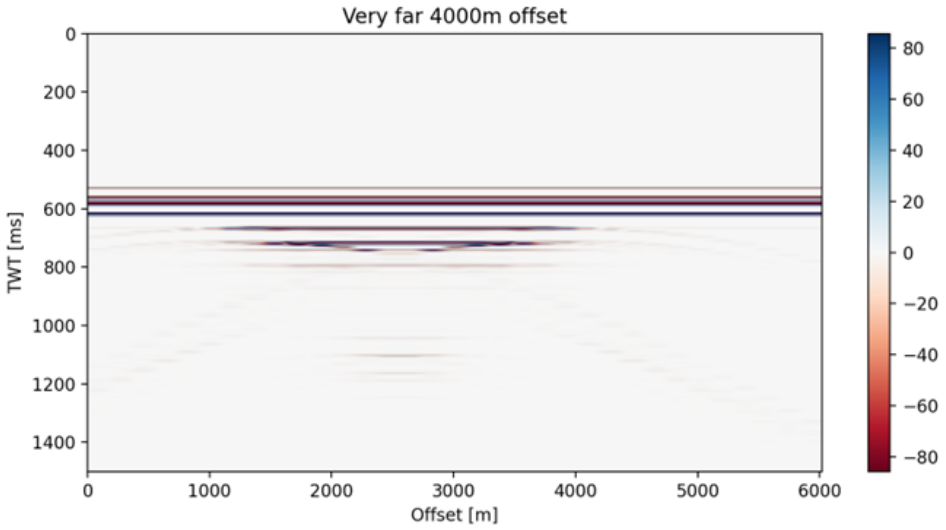

Figure 4.3.24: Very far offset section as 4000 m offset.

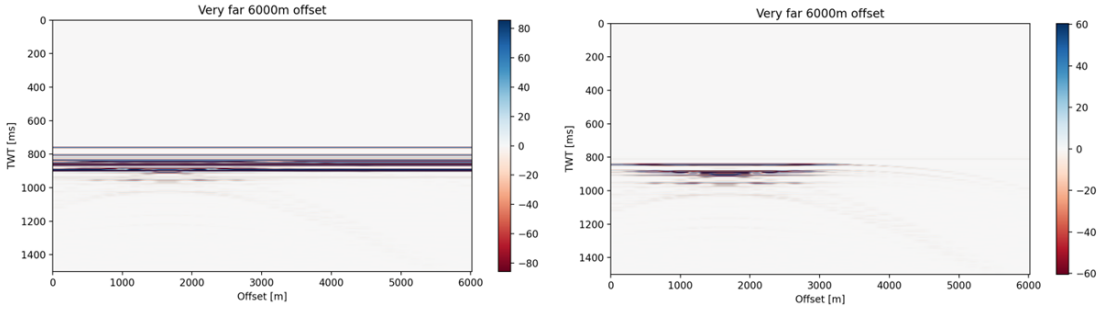

Figure 4.3.25: Very far offset section as 6000 m offset.

For very far offset as transmissions, a very far receiver as 4000 m and 6000 m was chosen. In addition, for better quality image, direct wave and seabed reflection in very far 6000 m offset were extracted. Because the direct wave and seabed reflections interfere the CO2 layer reflection.

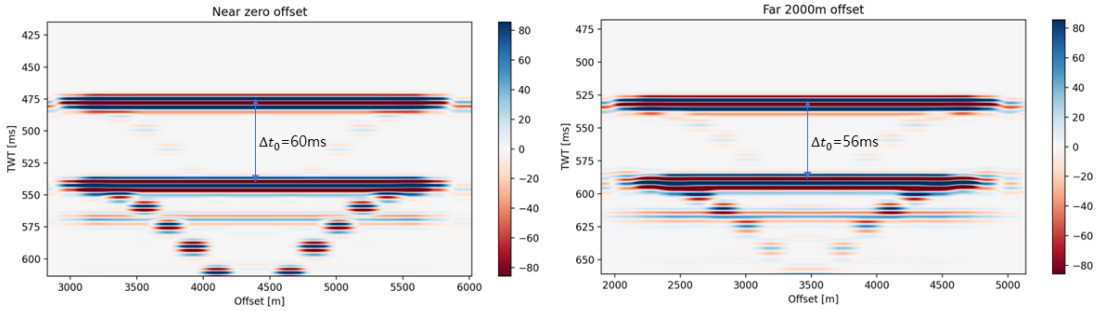

Figure 4.3.26: CO2 layer TWT difference between near and far offset.

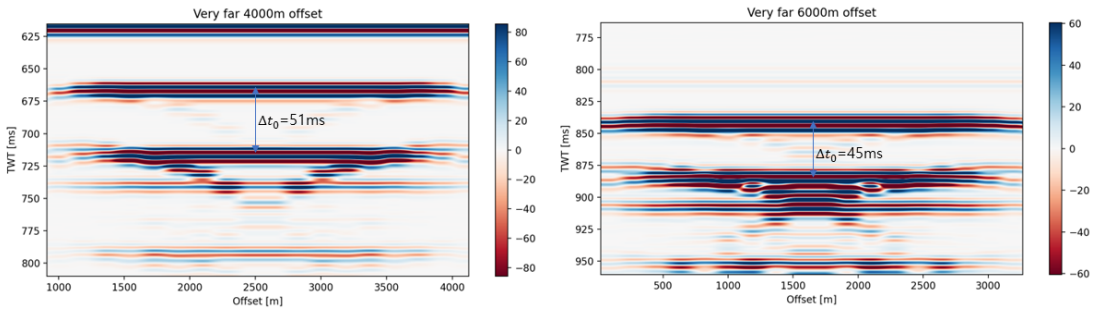

Figure 4.3.27: CO2 layer TWT difference between very far offsets.

In case of my near, far, very far offset sections, they showed the TWT from top to bottom of CO2 layer getting decreased. In addition, compared to true depth model, TWT of CO2 layer in shallower model decreases even more.

Using suitable algorithms and data processing techniques, the extraction of shot gathers and the determination of offsets were carried out. This analysis enabled a thorough comprehension of the seismic response and provided insight into the detection of CO2 layers in various acquisition configurations.

CHAPTER

FIVE

DISCUSSION

The analysis of the near, far, and very far offset sections revealed a consistent trend of decreasing two-way travel time (TWT) from top to bottom of the CO2 layer (Figure 5.0.1). Additionally, the TWT of the CO2 layer in the shallower model exhibited a further decrease compared to the true depth model (Figure 5.0.2). These observations can be attributed to the travel path of the seismic waves within the overburden layer [3].

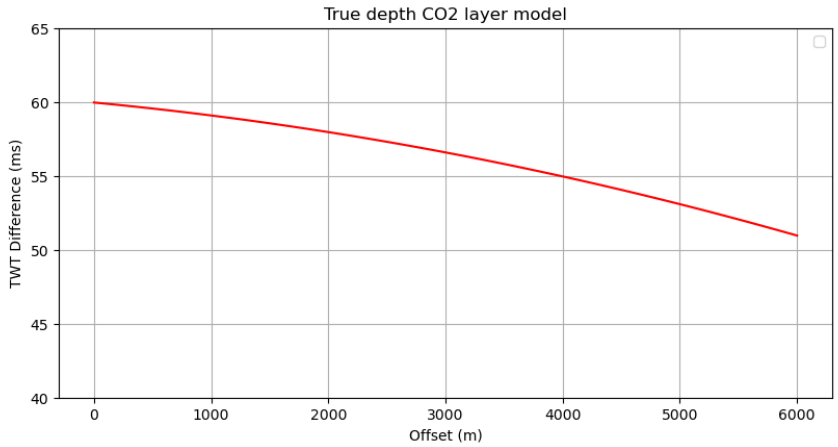

Figure 5.0.1: TWT difference of CO2 layer in true depth model.

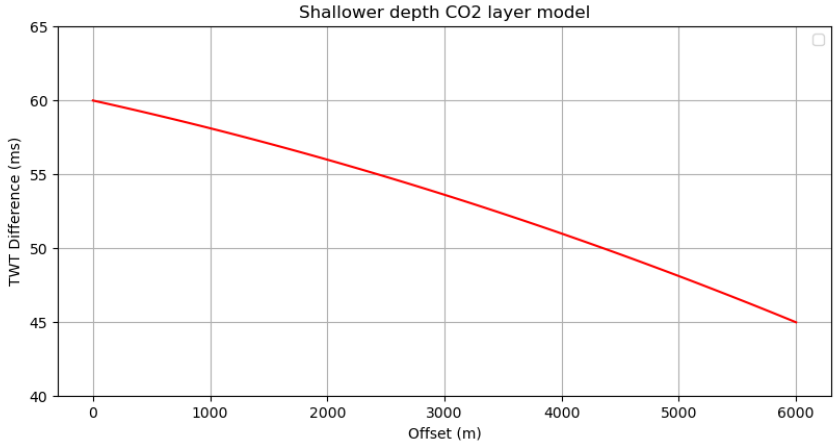

Figure 5.0.2: TWT difference of CO2 layer in shallower depth model.

The quality of the model and the theory used in this study have provided insights into the reflection of the seismic waves and detecting the CO2 layer. The decreasing TWT with increasing offset suggests that the seismic waves are traveling at more oblique angles through the CO2 layer, resulting in shorter path lengths and reduced travel times (Figure 5.0.3). This information is for understanding the subsurface properties and potential fluid reservoirs.

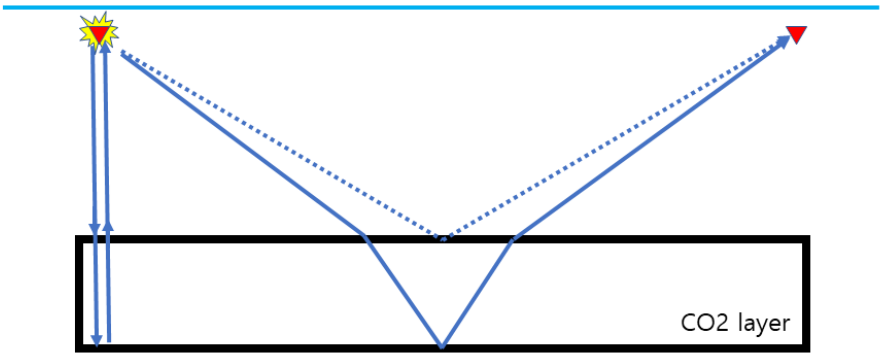

Figure 5.0.3: Comparing travel path over overburden layer and CO2 layer.

However, it is important to acknowledge some limitations and shortcomings associated with the model and the information applied in this study. The model relies on the simple velocity model which cannot represent real-world data. Moreover, rock properties, and seismic processing are not applied in this simple model. It may introduce uncertainties that can affect the accuracy of the TWT estimates.

To address these shortcomings and improve the quality of the study, future research should consider the following aspects. Firstly, applying rock properties based on real Sleipner filed data can help to have better characterize the subsurface layers, including the CO2 layer [14]. Additionally, interpolation and regularization methods can help address missing or incomplete data by estimating values at unsampled locations and mitigate uncertainties associated with the seismic data by providing a more coherent subsurface model. In addition, cost-effective modelling

should be considered. Computation time for running the model and the applied parameters inside the model, such as grid size, time step, spatial sampling for a model, maximum offset, etc would be taken into account.

CHAPTER

SIX

CONCLUSION

This study focused on seismic acquisition geometry on the detection of CO2 layers in three distinct scenarios. The velocity models were generated using the wave equation and specific parameters, providing insights into the behavior of CO2 within the subsurface. It is important to note that the models utilized in this study were based on a simplified environment, considering single sources and a simplified receiver configuration.

While the study acknowledged the cost-effectiveness of the chosen parameters such as grid size, time step, and spatial sampling, it is important to recognize the limitations in terms of the quality and accuracy of the results. The absence of detailed rock properties and comprehensive seismic processing techniques contributed to these limitations. However, despite these limitations, the study successfully demonstrated the basic concept of detecting CO2 layers and sequential CO2 injection phases.

Furthermore, the observed difference in two-way travel time (TWT) between the top and bottom of the CO2 layer provided valuable insights. The decrease in TWT with increasing offset indicated a shallower depth and shorter ray path, highlighting the importance of subsurface properties in the detection process. To achieve higher-quality output data, future studies should incorporate more comprehensive rock properties and seismic processing techniques.

While this study laid the foundation for understanding CO2 layer detection and sequential injection phases, further research is needed to enhance the quality and accuracy of the results.

REFERENCES

[1] Bastien Dupuy, Anouar Romdhane, Peder Eliasson, Etor Querendez, Hong Yan, Verónica A. Torres, and Amir Ghaderi, (2017), "Quantitative seismic characterization of CO2 at the Sleipner storage site, North Sea," Interpretation 5: SS23-SS42. doi:10.1190/INT-2017-0013.1
[2] Chadwick, Reid & Arts, R. & Eiken, Ola. (2005). 4D Seismic Quantification of a Growing CO2 Plume at Sleipner, North Sea. Petroleum Geology Conference series. 6. 10.1144/0061385.
[3] Audun Bakk, Rune M. Holt, Andreas Bauer, Bastien Dupuy and Anouar Romdhane (2015), Characterizing flow behavior for gas injection: Relative permeability of CO2-brine and N2-water in heterogeneous rocks, Water Resour. Res., 51, 9464–9489, doi:10.1002/2015WR018046.
[4] Trevisan, L., R. Pini, A. Cihan, J. T. Birkholzer, Q. Zhou, A. Gonzalez-Nicolas, and T. H. Illangasekare (2017), Imaging and quantification of spreading and trapping of carbon dioxide in saline aquifers using meterscale laboratory experiments, Water Resour. Res., 53, 485–502, doi:10.1002/2016WR019749.
[5] Williams, Gareth & Chadwick, Reid & Vosper, H.. (2018). Some thoughts on Darcy-type flow simulation for modelling underground CO 2 storage, based on the Sleipner CO 2 storage operation. International Journal of Greenhouse Gas Control. 68. 164-175. 10.1016/j.ijggc.2017.11.010.
[6] Martin Landrø (2011). Seismic Data Acquisition and Imaging, Trondheim, 4th August, 102 pages.
[7] Kearey, P., M. Brooks, and I. Hill (2009), An introduction to geophysical exploration.
[8] Öz Yilmaz (2001), Seismic Data Analysis: Processing, Inversion, and Interpretation of Seismic Data, Society of Exploration Geophysicists,
doi:10.1190/1.9781560801580.
[9] Sleipner Project. IEA Greenhouse Gas R&D Programme. Archived from the original on 2011-07-21. Retrieved 2009-12-26.
[10] Semere Solomon (2007), CO2 Storage: Case Study on the Sleipner Gas field in Norway, The Bellona Foundation.
[11] Enders A. Robinson and Sven Treitel (2008), Digital Imaging and Deconvolution: The ABCs of Seismic Exploration and Processing, Society of Exploration Geophysicists.
[12] Zadeh, H. M., and M. Landrø (2011), Monitoring a shallow subsurface gas flow by time-lapse refraction analysis: GEOPHYSICS, 76, O35–O43.
[13] Arts, R., O. Eiken, A. Chadwick, P. Zweigel, L. van der Meer, and B. Zinszner (2004), Monitoring of CO2 injected at Sleipner using time-lapse seismic data: En-

ergy, 29, 1383–1392.
[14] Chadwick, R., R. Arts, O. Eiken, G. Kirby, E. Lindeberg, and P. Zweigel (2004), 4d seismic imaging of an injected c02 plume at the sleipner field, central north sea: Geological Society, London, Memoirs, 29, 311-320.
[15] Ringrose, P., 2020. How to store CO2 underground: Insights from early-mover CCS Projects (Vol. 129). Cham, Switz: Springer.

Appendix

Skald script figure

```
#Creating true models for FWI. Max Offset 6 km. MaxDepth = 1.5 km
import numpy as np
import matplotlib.pyplot as plt

#Defining 1D model parameters
freq = 5
maxoff = 6
dm   = 0          # [m] Magnitude for model displacement to avoid top boundary artefacts
zb   = 70+dm        # [m] Depth of the water column
zmax = 1500         # [m] Max depth of model
dz   = 2            # [m] Z grid size for model
z    = np.arange(0,zmax+dz,dz) # [m] Depth vector
vw   = 1500         # [m/s]  Water column velocity
vp   = np.ones(np.shape(z))*vw
vo   = 1714         # [m/s]  Velocity at the seabed
g    = 0.5          # [s^-1] Velocity gradient for linear function
v    = lambda z: vo + (z-zb)*g # [m/s]  Linear velocity function
dz1  = 50           # [m] Thickness of thin layer 1
ztt1 = 800+dm         # [m] Top of thin layer 1
ztb1 = ztt1+dz1     # [m] Base of thin layer 1
ztt0 = ztt1-dm

#Defining velocities as in Landro 2021 for calculations.
c0 = vw
c1 = v(ztt1)                            #Velocity at the top of the thin layer from background model
c2 = v(ztb1)
cb = vo
cg = 1700

#Defining parameters for 2D model
dx     = 10                           #Spatial sampling X for model
dg     = dx
xmax   = 26000                        #Xmax for model dimensions
x      = np.arange(0,xmax+dx,dx)                #Spatial horizontal distance vector
velm   = np.zeros((np.size(z),np.size(x)))
xl1    = 11500                    #Location X of start edge of layer
l1     = 3000                         #Spatial extension of layer1 [0.5 1 3 5 10]
xl2    = xl1+l1                   #Location X of end   edge of layer
xlm1   = (xl1+xl2)/2                    #X value for midpoint of layer1

#Creating 1D linear model with water column and with encased thin layer
vp = v(z)
vb = v(z)
vp[z<zb]=vw
vb[z<zb]=vw
vp[(z>=ztt1) & (z<=ztb1)] = cg

#Creating 2D model
velm=np.tile(vb,np.size(x)) #Replicating Background model
velm=np.reshape(velm,[np.size(x),np.size(vp)])
velm=velm.transpose()

#Adding thin layer
velm[:,(x>=xl1) & (x<=xl2)]=np.reshape(np.tile(vp,np.size(np.arange(xl1,xl2+dx,dx))),-
  [np.size(np.arange(xl1,xl2+dx,dx)),np.size(vp)]).transpose()
velm = np.float32(velm)
velm = velm.flatten()

#Saving binary for velocity
file = open('/home/young/Documents/test1/models/vp-true.bin'.format(maxoff*1000), "wb")
file.write(velm)
file.close()

#Saving binary for density
velm = velm*0+1000; #If creating density
file = open('/home/young/Documents/test1/models/rho-true.bin'.format(maxoff*1000), "wb")
file.write(velm)
file.close()

data = np.fromfile('/home/young/Documents/test1/models/vp-true.bin'.format(maxoff*1000),dtype='float32')
# data = np.fromfile('/cluster/home/ricardm/Work/seiscode_new/diving_wave6/fwi_dz20_off%d_single_t1g10/models/rho-true.bin'%-
  (maxoff*1000),dtype='float32')

print('dx=%d, dz=%d, nx=%d, nz=%d,'%(dx,dz,int(data.size/(int(zmax/dz)+1)),int(zmax/dz)+1))

n1   = int(data.size/(int(zmax/dz)+1))          # Number of columns in matrix. Note that model is rotated 90 deg counterclockwise.
          # Hence it corresponds to the distance coordinate with model reference
n2   = int(data.size/n1)  # Number of rows in matrix. Correspond to Z in the model
dy   = dz
xmax = n1*dx
ymax = n2*dy
x    = np.arange(0,xmax,dx)
y    = np.arange(0,ymax,dy)
data = data.reshape(n2,n1)
#fig = plt.figure()
#p = 0.1
#ax = fig.add_axes([0+p,0+p,1-p,1-2*p])

#extent=rec[0], rec[-1], 0, 0.0008*7501

#extent = np.min(x), np.max(x), np.max(y), np.min(y)
#plt.imshow(X=data[:, ::2],extent=extent,cmap='jet')
#plt.colorbar()
#plt.clim([1500, 2900])
#plt.axis("auto")
#plt.xlabel('X [m]')
#plt.ylabel('Z [m]')
#plt.ylim((1000,0))

#plt.show()

#plt.imshow(X=data[:, ::10],cmap='jet')
#plt.colorbar()
#plt.axis("auto")
#plt.xlabel('X [m]')
#plt.ylabel('Z [m]')
#plt.show()
```

Figure .0.1: Python script for velocity model.

```
#!/bin/bash

#############################################################
#
# Generate wavelet, source and receiver, and finite difference
# parameters
#
# The density model is uniform 1000.0 kg/m^3
# S-wave velocity is zero
#
# Author: Ricardo Martinez <ricardo.m.guzman@ntnu.no>
# Date: Mai 24th 2022
#
#############################################################

#Wavelet and FD parameters
nt=7501    # number of time samples for 2 s record length
dt=0.001   # time step
t0=0.1      # shot time
f0=20       # central frequency
ns=33        # number of sources to use
free=1      # free surface
interp=0    # interpolation of sources and receivers
npml=20     # pml thickness
interprad=4 # interpolation radius

# Creating source
abpsource -o wavelet -n $nt -d $dt -f $f0 -t $t0
makeaxis --ofile fdtaxis.bin --n $nt --d $dt --o 0
echo "nt=$nt, dt=$dt"

#Creating source parameters
#python3 generate-sources.py

#Creating receiver parameters
python3 generate-rec-param.py
```

Figure .0.2: Skald script for geometry.

```
<?xml version="1.0"?>
<!DOCTYPE AKERBP-XML-SKALD "xml_skald.dtd">

<TITLE> Gullfaks data generation (acoustic) </TITLE>

<MODELS>
  <NXYZ> 2601, 751, 1  </NXYZ>              <!-- Sizes on models in order nx, ny, nz -->
  <DXYZ> 10.0, 10.0, 1.0 </DXYZ>            <!-- Sampling for models for x, y and z-axis -->
  <P1> ../models/rho-true.bin </P1>         <!-- Path to density model -->
  <P2> ../models/vp-true.bin </P2>          <!-- Path to Vp model -->
  <P3> ../models/eps-true.bin </P3>         <!-- Path to epsilon model -->
  <P4> ../models/del-true.bin </P4>         <!-- Path to delta model -->
  <PARAMETRIZATION> 0 </PARAMETRIZATION>    <!-- Which physics to use: 0=Isotropic acoustic, 100=VTI acoustic-->
</MODELS>

<FILES>
  <SRC> ../param/wavelet </SRC> <!-- Path to source wavelet -->
</FILES>

<DATA>
  <NT> 7501 </NT>   <!-- Number of samples in output data -->
  <DT> 0.001 </DT>  <!-- Sampling interval for output data-->
</DATA>

<PATH>
  <DATA> ../data-generation/Data/</DATA>  <!-- Path to where to store the data -->
</PATH>

<FD>
  <NPML> 20 </NPML>         <!-- Number of grid cells in PML area. 20 is a decent choice. -->
  <FREESURF> 1 </FREESURF>  <!-- If free surface should be included in modeling. 1 is free surface, 0 is absorbing surface -->
</FD>

<MOD>
  <SHOTS> 0,1,2,3,4,5,6,7,8,9,10,11,12,13,14,15,16,17,18,19,20,21,22,23,24,25,26,27,28,29,30,31,32 </SHOTS>
  <!-- Which shots to model -->
</MOD>
```

Figure .0.3: Skald script for executing file.